

**INTERNAL FLOW DYNAMICS IN LIQUID SWIRL INJECTORS WITH  
COAXIAL GAS FLOW**

A Dissertation  
Presented to  
The Academic Faculty

By

Matteo Trucchi

In Partial Fulfillment  
of the Requirements for the Degree  
Master of Science in the  
Daniel Guggenheim School  
Department of Aerospace Engineering

Georgia Institute of Technology

December 2023

© Matteo Trucchi 2023

**INTERNAL FLOW DYNAMICS IN LIQUID SWIRL INJECTORS WITH  
COAXIAL GAS FLOW**

Thesis committee:

Dr. Vigor Yang, Advisor  
School of Aerospace Engineering  
*Georgia Institute of Technology*

Dr. Adam Steinberg  
School of Aerospace Engineering  
*Georgia Institute of Technology*

Dr. Joseph Oefelein  
School of Aerospace Engineering  
*Georgia Institute of Technology*

Date approved: November 30, 2023

## TABLE OF CONTENTS

<b>List of Tables</b> . . . . .	v
<b>List of Figures</b> . . . . .	vi
<b>List of Acronyms</b> . . . . .	ix
<b>Summary</b> . . . . .	xiv
<b>Chapter 1: Introduction and Background</b> . . . . .	1
1.1 Introduction . . . . .	1
1.2 Background . . . . .	4
1.3 Research Objectives . . . . .	7
<b>Chapter 2: Theory of Liquid Monopropellant Swirl Injectors</b> . . . . .	9
2.1 Steady-State Theory of Swirl Injectors . . . . .	9
2.2 Linear Dynamics of Swirl Injectors . . . . .	19
2.2.1 Tangential Channels . . . . .	20
2.2.2 Swirling Chamber . . . . .	22
2.2.3 Transfer Function of Open-End Injectors . . . . .	28
<b>Chapter 3: Transfer Function of Open-Head Open-End Injectors</b> . . . . .	33
3.1 Forced Wave Equation . . . . .	34

3.2	Wave Equation Solution and Injector Transfer Function . . . . .	37
3.3	Inconsistencies in Previous Models . . . . .	40
3.4	Emulation of the Classical Theory . . . . .	43
3.4.1	Extended Theory . . . . .	44
3.4.2	Asymptotic Theory . . . . .	46
3.4.3	Optimized Extended Theory . . . . .	49
3.5	Parametric Study . . . . .	51
3.5.1	Injector Length . . . . .	52
3.5.2	Geometric Characteristic Parameter . . . . .	53
3.5.3	Pressure Drop . . . . .	54
3.5.4	Gas Velocity . . . . .	56
<b>Chapter 4: Numerical Investigation . . . . .</b>		<b>58</b>
4.1	Preliminary Study . . . . .	58
4.2	Geometry and Mesh . . . . .	63
4.3	Solver Setup . . . . .	65
4.3.1	Numerical Models . . . . .	65
4.3.2	Boundary Conditions . . . . .	66
4.4	Numerical Results . . . . .	67
<b>Chapter 5: Results and Conclusions . . . . .</b>		<b>74</b>
5.1	Future Work . . . . .	76
<b>References . . . . .</b>		<b>78</b>

## LIST OF TABLES

3.1	Injector configurations employed for the comparative analysis between the extended and classical theory . . . . .	44
3.2	Tuning coefficients for different injector lengths . . . . .	52
3.3	Tuning coefficients for different values of the geometric characteristic parameter . . . . .	53
3.4	Tuning coefficients for different values of the injector pressure drop . . . . .	55
4.1	OHOE injector configuration . . . . .	59
4.2	Theoretical and numerical swirling radius of the liquid surface . . . . .	59

## LIST OF FIGURES

1.1	Illustration of a closed-end swirl injector . . . . .	1
1.2	Scheme of the dynamic interactions involving the injector element . . . . .	2
1.3	Illustration of Open-Head Open-End swirl injector with axial gas flow . . . . .	7
2.1	Discharge coefficient as function of the coefficient of passage fullness . . . . .	14
2.2	Dimensionless parameters as a function of the geometric characteristic parameter . . . . .	17
2.3	Transfer function diagram for short jet injectors . . . . .	22
2.4	Theoretical Validation – Amplitude and phase diagrams of the injector transfer function as a function of frequency for different values of injector length to diameter ratio . . . . .	31
2.5	Theoretical Validation – Amplitude and phase diagrams of the injector transfer function as a function of frequency for different values of the geometric characteristic parameter . . . . .	32
3.1	Schematic representation of OHOE injector at steady-state . . . . .	34
3.2	Illustration of the shear stress acting on the liquid film . . . . .	35
3.3	Impact on transfer function when accounting for mean axial liquid velocity in the wave propagation speed . . . . .	41
3.4	Impact on transfer function when not accounting for mean axial liquid velocity . . . . .	42
3.5	Impact on transfer function when removing the damping term in $\Pi_{vcIII}$ . . . . .	43

3.6	Extended vs Classical Theory – Amplitude and phase diagrams with $L_{vc} = 75$ mm . . . . .	45
3.7	Extended vs Classical Theory – Amplitude and phase diagrams with $L_{vc} = 7$ mm . . . . .	45
3.8	Extended vs Classical Theory – Amplitude and phase diagrams with $A = 10$ and $A = 4$ . . . . .	46
3.9	Evolution of $Z_1$ and $Z_2$ as a function of frequency . . . . .	47
3.10	Extended vs Asymptotic Theory – Injector transfer function on the complex plane . . . . .	48
3.11	Impact of the asymptotic theory on the injector transfer function at low frequencies . . . . .	48
3.12	Asymptotic Theory – Impact of injector length on the injector transfer function . . . . .	49
3.13	Optimized Theory – Impact of injector length on the injector transfer function	51
3.14	Optimized Theory Parametric Study – Impact of injector length on the injector transfer function . . . . .	52
3.15	Tuning coefficients as a function of $d_{vc}$ . . . . .	54
3.16	Optimized Theory Parametric Study – Impact of geometric characteristic parameter on the injector transfer function . . . . .	54
3.17	Tuning coefficients as a function of $\Delta p_{inj}$ . . . . .	55
3.18	Optimized Theory Parametric Study – Impact of injector pressure drop on the injector transfer function . . . . .	56
3.19	Optimized Theory Parametric Study – Impact of gas velocity on the injector transfer function . . . . .	57
4.1	Validation against Chen’s results with RSM . . . . .	60
4.2	Turbulence models on Chen’s injector . . . . .	60
4.3	a) Volume fraction in Chen’s injector for different turbulence models . . . . .	61

4.4	b) Volume fraction in Chen’s injector for different turbulence models . . . . .	62
4.5	Inviscid CHOE injector . . . . .	62
4.6	Injector domain and downstream region . . . . .	63
4.7	Coarse mesh . . . . .	64
4.8	Fine mesh with inflation layers . . . . .	64
4.9	Zoom on mesh refinement at the liquid-gas interface . . . . .	66
4.10	Instantaneous volume fraction snapshots with coarse mesh . . . . .	68
4.11	Instantaneous volume fraction snapshots with medium and fine mesh . . . . .	69
4.12	Cell distribution of $y^+$ . . . . .	70
4.13	Instantaneous volume fraction – $k - \omega$ SST – fine mesh – $W_g = 150$ m/s . . . . .	70
4.14	Instantaneous vorticity magnitude and pressure . . . . .	71
4.15	Time-averaged liquid surface for different turbulence models and grids . . . . .	72
4.16	Water time-averaged streamlines . . . . .	73

## **LIST OF ACRONYMS**

- CFD** Computational Fluid Dynamics
- CHCE** Closed-Head Closed-End
- CHOE** Closed-Head Open-End
- LRE** Liquid Rocket Engines
- MFR** Momentum Flux Ratio
- OHOE** Open-Head Open-End
- RANS** Reynolds-Averaged Navier–Stokes
- RNG** Re-Normalization Group
- RSM** Reynolds Stress Model
- SST** Shear Stress Transport

## NOMENCLATURE

### Physical and geometrical parameters

$\dot{m}$	Mass flow rate
$A$	Geometric characteristic parameter
$a$	Dimensionless parameter $a = 2(1 - \phi)^2 / (2 - \phi)$
$b$	Dimensionless parameter $b = a / (1 - \phi)$
$D$	Diameter
$F$	Area
$f$	Frequency
$g$	gravitational acceleration; centrifugal acceleration
$h$	Shallow water depth; liquid film effective thickness
$L$	Length
$n$	Number of tangential channels
$p$	Pressure
$Q$	Liquid volumetric flow rate
$R$	Radius of injector element, radial position
$r$	Radial location of liquid element, channel radius

$Sh$	Strouhal number
$t$	Time
$W$	Velocity
$z$	Axial direction
$\alpha$	Spray cone angle
$\Delta p$	Pressure drop
$\mu$	Discharge coefficient
$\nu$	Viscosity
$\Omega$	Amplitude of liquid film thickness fluctuation
$\omega$	Angular frequency
$\Phi$	Phase shift angle of a single process
$\phi$	Coefficient of passage fullness: portion of the nozzle area filled with liquid
$\Pi$	Transfer function, output/input
$\Psi$	Phase shift angle between injector parts
$\rho$	Density
$\tau$	Shear stress
$\xi$	Instantaneous fluctuation of liquid film thickness

### **Subscripts**

$\Sigma$	Total value
----------	-------------

$a$	Axial component
$ae$	Axial component at the nozzle exit
$am$	Axial component on the liquid surface
$an$	Axial component in the nozzle
$av$	Axial component in the vortex chamber
$e$	Nozzle exit
$f$	Manifold
$g$	Gas flow
$i, inj$	Injector
$in$	Inlet channel
$J$	Jet injector
$k$	Head end of the vortex chamber
$lg$	Liquid-gas
$lw$	Liquid-wall
$m$	Liquid vortex surface
$mk$	Liquid vortex surface at the head end of the vortex chamber
$mn$	Liquid vortex surface in the nozzle
$mv$	Liquid vortex surface in the vortex chamber
$n$	Nozzle
$r$	Radial component

$sh$	Shallow-water wave
$T$	Tangential inlet
$u$	Circumferential component
$ue$	Circumferential component at the nozzle exit
$um$	Circumferential component on the liquid surface
$un$	Circumferential component in the nozzle
$uv$	Circumferential component in the vortex chamber
$vc$	Vortex chamber
$vL$	Long vortex chamber
$w$	Wave

### **Superscripts**

$\overline{(\cdot)}$	Dimensionless parameter
$\tilde{(\cdot)}$	Instantaneous quantity
$(\cdot)'$	Pulsation component

## SUMMARY

Injectors are essential components in aerospace propulsion systems, serving a crucial role in achieving high-quality propellant atomization and mixing, as well as engine stability. They are integral components within a complex dynamic system and are responsible for coupling the feed system to the combustion chamber. Thus, a profound understanding of injector dynamics is imperative to attain a robust engine design.

Since the early studies, the typical configurations of interest have involved closed-head injectors, where the liquid propellant swirls around a stationary gas core. Gas-liquid interactions were introduced with recessed coaxial swirl injectors and air-blast injectors with major emphasis on the atomization process. The classical theory on injector dynamics lacks the consideration for the effect of the shear stress at the liquid-wall and gas-liquid interfaces in the governing equations. Therefore, the damping effect on propagating waves is modelled exclusively through an artificial viscosity factor.

This work conducts a theoretical and numerical investigation for an alternative configuration of open-end swirl injectors. The distinctive feature of this configuration is an open head and a high speed gas that flows coaxially with the swirling liquid towards the injector exit. Unlike a recessed coaxial injector, the gas immediately interacts with the tangentially injected liquid into the chamber where the gas is flowing. The comprehensive review of classical steady-state and transient theories on swirl injectors led to the identification and resolution of inconsistencies. The analytical inclusion of shear stress at the liquid-wall and gas-liquid interfaces produced a modified wave equation, and the new solution was employed to extend the classical theory to Open-Head-Open-End injectors. A parametric study for frequencies up to 2000 Hz involving gas flow velocity, injector pressure drop, and geometric parameters highlighted the significance of friction coefficients tuning for an accurate calculation of the injector transfer function. Computational Fluid Dynamics provided a qualitative description of the flow physics involved in the injector configuration of interest.



processes [3]. The inlet channels are the first elements encountered by the propellant in its path towards the combustion chamber. Inlet channels are tangential to the vortex chamber, that is partially filled with swirling liquid and has a gas core around its symmetry axis. At the head-end of the vortex chamber, the liquid has only a tangential velocity component and the distance between the free surface and the symmetry axis is minimum. Note that the gas core must exist because the swirling velocity approaches infinity as the swirling radius tends to zero for angular momentum conservation. Proceeding towards the nozzle, the liquid gains axial velocity, therefore reducing the tangential component for energy conservation. Simultaneously, the swirling radius of the free surface increases for angular momentum conservation. The axial velocity is assumed to be constant and uniform within the vortex chamber, except at the head-end, where it attains a zero value. Exiting the vortex chamber, a conical convergent passage reduces the flow area and causes the flow to gain a high axial velocity. As a consequence, the swirling radius increases again. Finally, at the nozzle exit, the combination of the tangential and axial velocity produces a cone shaped thin layer of liquid. The liquid layer breaks down more downstream due to aerodynamic forces allowing atomization and mixing.

Swirl injectors are characterized by intrinsic non-stationary processes coupled with other elements of the engine. This renders injectors fundamental members of a complex dynamic system. A simplified scheme is shown in Figure 1.2, illustrating three primary interactions.

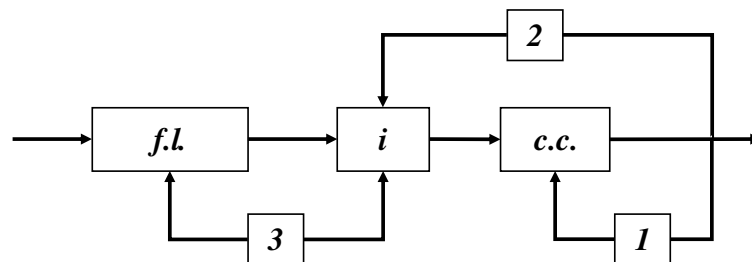


Figure 1.2: Simplified scheme of dynamic interactions between the injector (i), combustion chamber (c.c.), and feed line (f.l.).

Firstly, oscillations of the combustion chamber pressure impact the processes within the

chamber (1), specifically atomization, mixing and combustion. Concurrently, these pressure disturbances induce oscillations in velocity, and therefore, mass flow rate, within the injector element (2). Consequently, pressure fluctuations emerge in the feedline (3), given the interdependence of these two quantities. Fluctuations in the feed system combine with pressure oscillations generated by turbulent flows in pipes and valve vibrations. This combination significantly influences propellant injection. Clearly, the injector is the element that couples the feed system to the combustion chamber and it can be used to affect the engine dynamic system.

The initial investigations focused on closed-end swirl injectors, characterized by a convergent section connecting the vortex chamber to the nozzle. Conversely, the most recent configurations feature a vortex chamber extending up to the injector exit, referred as open-end swirl injectors. Both these injector types have a closed head-end and the gaseous core has no axial velocity. For rocket engines applications, an axial gas flow was introduced with recessed coaxial swirl injectors. In aeronautical combustors, instead, air-blast injectors are used. In particular, in pre-filming air-blast injectors the gas interacts with the liquid film formed on impingement plates, therefore promoting atomization.

The objective of this work is to conduct a theoretical and numerical study on a new class of coaxial swirl injectors featuring an open head. The liquid is tangentially injected into the duct where the gas is axially flowing at high speeds. Consequently, the gas interacts with the liquid from the outset. This investigation extends the classical theory on injector dynamics by incorporating additional physical phenomena that were absent in previous models and are relevant in Open-Head Open-End (OHOE) swirl injectors. An analysis is conducted to study the impact of geometric parameters and flow variables on the dynamic response of the injector. Finally, Computational Fluid Dynamics (CFD) provides a qualitative description of the flow physics in OHOE injectors. The presence of a high speed axial gas flow renders these injectors suitable for gas-turbine engines.

## 1.2 Background

The importance of controlling instabilities generated in LRE led to several studies about the internal flow dynamics of liquid swirl injectors. The early theoretical studies emerge in Russia with Bazarov [5] who focused his research on the flow dynamics in closed-end swirl injectors. Bazarov developed a linear theory based on the propagation of small disturbances in the flow, specifically surface waves and vorticity waves. The fluid is assumed to be inviscid, incompressible, and with no surface tension. Due to the linearity of his theory, Bazarov derived an analytical expression for the transfer function of the whole injector as a product of the response function of different injector parts. Several groups of researchers advanced the understanding of swirl injectors from a numerical, experimental and theoretical standpoint.

In Seoul National University in South Korea Prof. Youngbin Yoon and his group of researchers collaborated with Bazarov to investigate the effect of different geometries on the dynamic characteristics of a simplex injector [6]. They produced pressure oscillations in the feed line with a pulsator and measured the mass flow rate fluctuations as the output parameter. They found that the oscillations amplitude decreases with the decrease of the swirl chamber diameter and with the increase of the swirl chamber length, therefore achieving a more stable configuration. Moreover, the phase moves clockwise in the phase-amplitude diagram as the frequency of the input fluctuations increases. More parameters were analyzed in [7], where it was found that the phase diagrams of the pressure, axial velocity and mass flow rate start from the fourth quadrant and move in a clockwise direction, while the film thickness starts in the first quadrant. The quantification of the mass flow rate variation due to pressure fluctuations was investigated by Khil et al. [8] and a new method that uses pressure and film thickness in the nozzle was developed. Further studies by Chung et al. [9] focused on the dynamics of open-end swirl injectors. It was found that there exists a direct proportionality between the liquid film thickness fluctuation at the exit of the injector and

the input pressure oscillation amplitude. However, the increase of tangential inlet number, vortex chamber diameter and length lowers the proportionality coefficient. Several studies were also conducted about the self-pulsation phenomenon, first by V. Bazarov and V. Yang [4] and then in South Korea [10–12], where the effect of internal flow dynamics on spray characteristics and liquid sheet break up were additional topics of interest [13–17].

In the USA, Prof. S. Heister at Purdue University focused his efforts on numerical investigation and led his research team to undertake extensive simulations. They used the Boundary Element Method (BEM) to explore the nonlinear dynamic response of swirl injectors [18]. Ismailov et al. [19–21] have deconstructed the entire unsteady flow phenomena within swirl injectors into distinct components: disturbance wave refraction, wave reflection, and vortex chamber resonance. This deconstruction served as the basis for their linear small perturbation analysis. Furthermore, Ismailov conducted dynamic simulations using the nonlinear BEM, revealing that the peak of dynamic responses aligns precisely with resonant frequencies. Richardson et al. [22], instead, engaged in a comparative study by contrasting simulation outcomes obtained through the BEM with those originating from Bazarov's linear model. This analysis demonstrated a notable level of agreement for frequencies below 5000 Hz. Beyond this threshold, discrepancies started to emerge between the two models.

In Beijing University of Astronautics and Aeronautics, Fu et al. [23–25] investigated the dynamics in open-end injectors and observed that the magnitude of the film thickness fluctuation diminishes as the frequency of pressure oscillation rises. Additionally, they noted that the frequency of the fluctuation in film thickness aligns with the frequency of pressure oscillation. Furthermore, they established a direct linear relationship between the phase disparity of mass flow rate fluctuation and pressure oscillation when the pressure oscillation frequency increases. Moreover, the researchers found that the phase contrast is influenced by two factors: the geometric characteristic constant  $A$ , and the pressure drop. They observed that an increase in the value  $A$  leads to a rise in the phase contrast, while

an increase in the pressure drop results in a reduction of the phase contrast. Starting from the transfer function for closed injectors derived by Bazarov, L. Yang et al. [26] derived the transfer function of an open-end injector. They considered no wave reflection due to the absence of a converging conical section, which is responsible of reflecting disturbance waves back to the head-end of the injector. Moreover, they derived the transfer function of a swirl injector with two rows of tangential channels. They discovered that oscillations are attenuated under the condition where the distance between the rows equals half of a disturbance wavelength. This damping effect arises due to the opposite phase of surface waves generated by the two inlet rows. Similarly, Richardson, Zakharov and Heister [22, 27] observed that pressure swirl injectors featuring double rows of inlets exhibit more favorable stability traits compared to their single-row counterparts due to the possibility of wave cancellation with the appropriate tuning.

Additional configurations of interest in LRE include gas and liquid centered coaxial swirl injectors. Fu et al. derived the analytical expression for the transfer function in a recessed liquid centered coaxial swirl injector [28], while experimental studies were conducted by Park et al. on gas centered injectors with a pulsating gas and liquid flow [29, 30]. The latter measure the injector transfer function for different recess ratios, momentum flux ratios, and gap thickness between the liquid inlet and the solid surface extending up to the area of liquid-gas contact. The gap and the momentum flux ratio have a significant impact on the liquid oscillations. Other investigations conducted in China, instead, focused on the atomization characteristics of this type of injectors [31, 32].

In aeronautical gas turbine engines, much attention was placed on air-blast atomizers. Investigations focus on atomization process, breakup of the liquid film, prediction of drop sizes and trajectories with the main objective of spray characterization. Studies were conducted under the theoretical, numerical and experimental perspective [33–43].

### 1.3 Research Objectives

Previous studies on swirl injectors mainly focus on configurations featuring a closed-head end and a liquid film swirling around a stationary gas core. When an axial gas flow is introduced, the typical configurations of interest include recessed coaxial swirl injectors for LRE and air-blast injectors for air-breathing engines.

The aim of this work is to theoretically and numerically investigate a new class of coaxial swirl injectors, schematically depicted in Figure 1.3. The alternative configuration entails an injector design with openings at both ends (OHOE). The liquid is tangentially injected into the duct where the gas is axially flowing at high speeds. The interaction between the two phases is immediate and not limited to a specific region as in recessed swirl injectors.

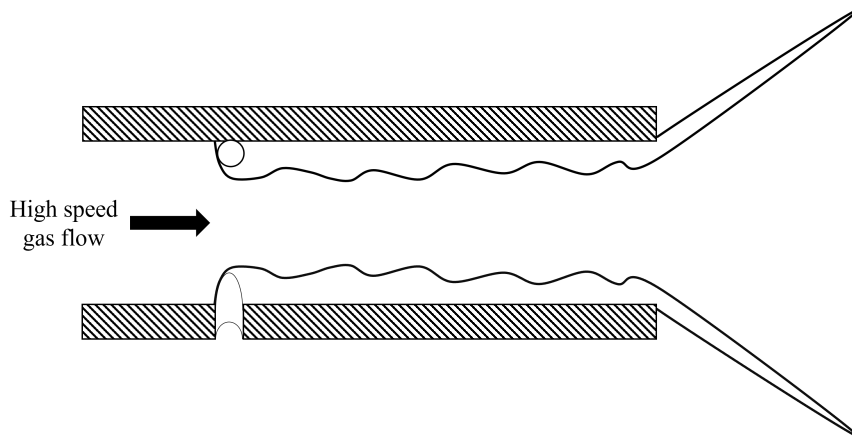


Figure 1.3: Illustration of Open-Head Open-End swirl injector with axial gas flow.

The study of this configuration requires the consideration of additional physical phenomena, not included in previous models. The classical model is extended to analytically include the effect of shear stress at the liquid-wall and gas-liquid interfaces in the governing equations. These changes lead to the derivation of a modified wave equation and a new solution. The latter is employed to apply changes to the classical injector transfer function. Unlike previous models that are based on artificial viscosity factors, the disturbances undergo a damping effect analytically represented. A parametric study involving

geometric parameters, gas flow velocity and injector pressure drop for frequencies up to 2000 Hz is performed to analyze the effect on the injector transfer function. Furthermore, the parametric study highlights the significance of friction factors calibration for the accurate calculation of the injector response function. Finally, CFD simulations aid in the qualitative description of the flow physics in OHOE injectors.

For the sake of comprehensiveness, this work presents the steady-state theory of swirl injectors from Ref. [3] to emphasize the most important parameters and their mutual relation. The analysis of the linear dynamics from Bazarov's theory [5, 44] and the review of the transfer function derivation for open-end swirl injectors outlined in [26] facilitated the detection and resolution of typographical errors and inconsistencies.

## CHAPTER 2

### THEORY OF LIQUID MONOPROPELLANT SWIRL INJECTORS

#### 2.1 Steady-State Theory of Swirl Injectors

The classical theory describing the ideal steady state flow in a swirl injector is fundamental to understand the effect of geometrical and physical parameters on the flow. The approach followed in Ref. [3] is of great help to establish all the important relations to produce the preliminary design of a liquid swirl injector.

The entire theory is based on the following principles: conservation of mass, energy and angular momentum, Bernoulli's equation and maximum flow. The liquid propellant enters the vortex chamber of the injector through tangential inlets with a velocity  $W_{in}$ . The purely swirling flow gains axial velocity until it exits the injector from the nozzle generating a conic liquid sheet. The latter breaks down into droplets ensuring atomization of the liquid. The liquid propellant swirls around a stationary gas core such that the pressure on the liquid free surface is equal to the pressure in the combustion chamber. Through the Bernoulli's equation it is obvious how the pressure difference across the injector is converted into flow velocity, meaning that the potential energy is converted into kinetic energy. Therefore, the total liquid flow velocity on the free surface is

$$W_{\Sigma} = \sqrt{\frac{2}{\rho}\Delta p_i} = \sqrt{2(p_f - p_c)/\rho} \quad (2.1)$$

where  $p_c$  is the combustion chamber pressure and  $p_f$  is the pressure in the propellant feed system upstream the tangential entries. In the same way, the inlet velocity can be obtained

$$W_{in} = \sqrt{2(p_f - p_{in})/\rho} \quad (2.2)$$

where  $p_{in}$  is the tangential inlet pressure. Assuming that the radial velocity in the liquid film is negligible, then  $W_r = 0$  and the total velocity is

$$W_{\Sigma} = \sqrt{W_u^2 + W_a^2} \quad (2.3)$$

where the subscripts  $u$  and  $a$  refer to the circumferential and axial velocity, respectively. The axial velocity at the head end of the vortex chamber  $W_{ak}$  is also zero, thus

$$W_{\Sigma} = W_{uk} \quad (2.4)$$

where the subscript  $k$  denotes the injector head end.

The conservation of angular momentum gives

$$W_{in}R_{in} = W_{uk}r_{mk} = W_{un}r_{mn} = W_{um}r_m \quad (2.5)$$

with  $R_{in}$  the radial location of the center of tangential inlets from the symmetry axis, and the subscripts  $m$  and  $n$  referring to the liquid free surface and the nozzle section, respectively. The existence of a free surface that separates the liquid flow from a gas core is ensured by the conservation of angular momentum. According to Equation (2.5) the swirling liquid would approach infinite velocity as  $r_m$  goes to zero, thus the injector cannot be filled with liquid. In addition, for the same principle,  $r_{mk}$  is the minimum swirling radius: the entire kinetic energy is represented by the swirling motion at the head end. The swirling radius increases with the increase of axial velocity of the fluid to conserve both energy and angular momentum.

The coefficient of passage fullness is defined as the ratio between the area filled by the liquid and the nozzle area

$$\phi = \frac{\pi(R_n^2 - r_{mn}^2)}{\pi R_n^2} = 1 - \frac{r_{mn}^2}{R_n^2} \quad (2.6)$$

where  $R_n$  is the nozzle radius and  $r_{mn}$  the liquid film radius in the nozzle. Moreover, the flow discharge coefficient  $\mu$  is defined as the ratio between the actual mass flow rate and the maximum flow rate through the nozzle

$$\mu = \frac{\rho W_{an} F_n \phi}{\rho W_{\Sigma} F_n} = \frac{W_{an} \phi}{W_{\Sigma}} \quad (2.7)$$

where  $F_n$  is the nozzle area. Using Equations (2.3) and (2.5), Equation (2.7) can be written as

$$\mu = \phi \sqrt{\frac{W_{\Sigma}^2 - W_{un}^2}{W_{\Sigma}^2}} = \phi \sqrt{1 - \frac{r_{mk}^2}{r_{mn}^2}} \quad (2.8)$$

The most important parameter is the injector geometric characteristic

$$A = \frac{F_n R_{in}}{F_{in} R_n} = \frac{R_{in} R_n}{n r_{in}^2} \quad (2.9)$$

where  $F_{in}$  is the total area of the inlet channels,  $n$  is the number of tangential inlets,  $r_{in}$  is the radius of the inlet channels and the other parameters are defined above. In addition, the liquid sheet spreading angle at the nozzle exit is

$$\tan \alpha = \frac{W_{un}}{W_{an}} \quad (2.10)$$

An additional equation can be derived exploiting a differential volume approach as follows. Considering a liquid element at radius  $r$  with unit thickness, width  $dr$  and length  $r d\theta$  and equating the pressure and centrifugal forces, the following expression is obtained

$$r d\theta dP = dm \frac{W_u^2}{r} \quad (2.11)$$

where  $P = p - p_c$ , and  $W_u$  and  $r$  refer to the liquid element in the liquid film. Using the

conservation of angular momentum within the liquid film

$$W_u = \frac{W_{um}r_m}{r} \quad (2.12)$$

and noting that  $dm = \rho r dr d\theta$ , Equation (2.11) becomes

$$dP = \rho W_{um}^2 r_m^2 \frac{dr}{r^3} \quad (2.13)$$

This expression can be integrated with  $P = 0$  at  $r = r_m$  since  $p = p_c$  on the surface. As a result

$$P = \frac{\rho}{2}(W_{um}^2 - W_u^2) \quad (2.14)$$

The Bernoulli's equation leads to

$$\frac{\rho}{2}(W_a^2 + W_u^2) + P = P_t \quad (2.15)$$

where  $P_t = p_f - p_c$ . Substitution of Equation (2.14) into Equation (2.15) yields

$$W_a = \sqrt{\frac{2P_t}{\rho} - W_{um}^2} \quad (2.16)$$

From Equation (2.5)

$$W_{um} = \frac{W_{in}R_{in}}{r_m} \quad (2.17)$$

The total volumetric flow rate entering the vortex chamber through the tangential passages is given by

$$Q = n\pi r_{in}^2 W_{in} \quad (2.18)$$

Finally, substituting  $W_{in}$  from Equation (2.18) into Equation (2.17) and then using the latter

to substitute  $W_{um}$  in Equation (2.16), the following expression is derived

$$W_a = \sqrt{\frac{2P_t}{\rho} - \frac{R_{in}^2 Q^2}{n^2 \pi^2 r_{in}^4 r_m^2}} \quad (2.19)$$

This expression can be substituted in the following equation for the liquid flow rate

$$Q = \phi \pi R_n^2 W_a \quad (2.20)$$

Equating  $W_a$  from Equations (2.19) and (2.20) and using Equation (2.9), the liquid flow rate can be expressed as

$$Q = \frac{1}{\sqrt{\frac{A^2}{1-\phi} + \frac{1}{\phi^2}}} \pi R_n^2 \sqrt{\frac{2P_t}{\rho}} \quad (2.21)$$

where the last term under the square root represents the total velocity and its multiplication with the nozzle area  $F_n = \pi R_n^2$  gives the maximum possible volumetric flow rate in the nozzle. Therefore, based on the definition of the flow coefficient  $\mu$  and from Equation (2.21), it is possible to write

$$\mu = \frac{1}{\sqrt{\frac{A^2}{1-\phi} + \frac{1}{\phi^2}}} \quad (2.22)$$

From the physical standpoint, the increase of  $\phi$  causes the axial velocity to decrease faster than the increase of the equivalent flow area, therefore the mass flow rate decreases. The decrease of  $\phi$ , instead, causes the equivalent flow area to decrease faster than the increase in axial velocity, thus the mass flow rate decreases also in this case. As a consequence, a maximum must exist and it is found applying the following condition to Equation (2.22)

$$\frac{d\mu}{d\phi} = -\frac{1}{2} \left( \frac{A^2}{1-\phi} + \frac{1}{\phi^2} \right) \left( \frac{A^2}{(1-\phi)^2} - \frac{2}{\phi^3} \right) = 0 \quad (2.23)$$

The latter expression allows to express the geometric characteristic parameter as a function

of the coefficient of passage fullness as follows

$$A^2 = \frac{2(1 - \phi)^2}{\phi^3} \quad (2.24)$$

Substituting Equation (2.24) into Equation (2.22) leads to the optimum value of  $\mu$ , that is

$$\mu = \phi \sqrt{\frac{\phi}{2 - \phi}} \quad (2.25)$$

The mass flow coefficient as a function of  $\phi$  for different values of  $A$  is shown in Figure 2.1, where the dashed line is from Equation (2.25) and the other curves are from Equation (2.22).

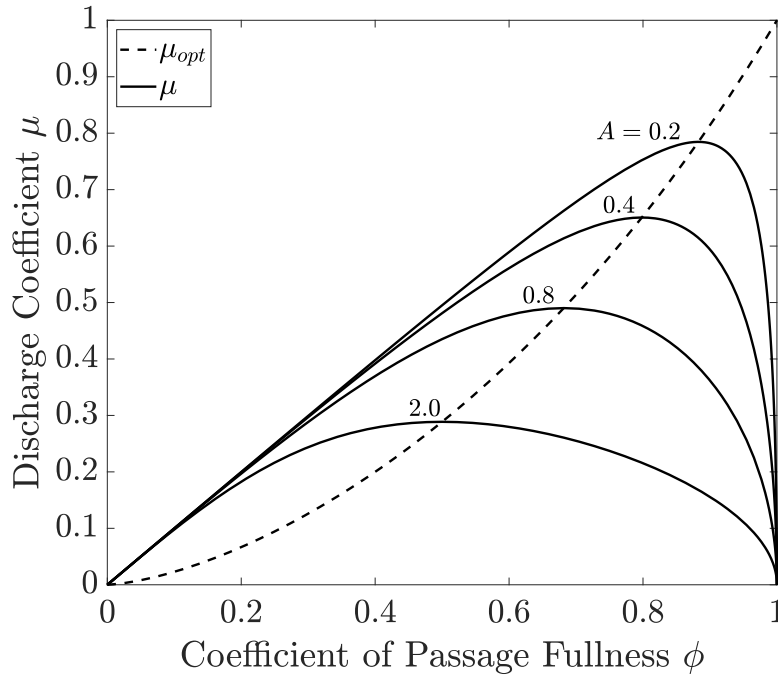


Figure 2.1: Discharge coefficient  $\mu$  as a function of the coefficient of passage fullness  $\phi$  for different values of the geometric characteristic parameter  $A$ . The dashed line is the optimum discharge coefficient  $\mu_{opt}$ .

It is possible to find the relation between the pressure drop across the tangential channels  $\Delta p_{in}$  and across the whole injector  $\Delta p_i$ . From Equations (2.1) and (2.7), the axial velocity

in the nozzle can be written as

$$W_{an} = \frac{\mu}{\phi} \sqrt{\frac{2}{\rho}(p_f - p_c)} \quad (2.26)$$

The circumferential velocity at a radius  $r_m$  is given by the conservation of angular momentum in Equation (2.5) and the inlet velocity in Equation (2.2):

$$W_{um} = \frac{r_{mk}}{r_m} W_{\Sigma} = \frac{R_{in}}{r_m} W_{in} = \frac{R_{in}}{r_m} \sqrt{\frac{2}{\rho}(p_f - p_{in})} \quad (2.27)$$

Applying the Bernoulli's equation at the nozzle section, the total pressure in the manifold is

$$p_f = p_c + \frac{\rho}{2}(W_{un}^2 + W_{an}^2) \quad (2.28)$$

Substituting Equations (2.26) and (2.27) into Equation (2.28) yields

$$p_f - p_c = \frac{\mu^2}{\phi^2}(p_f - p_c) + \frac{R_{in}^2}{r_{mn}^2}(p_f - p_{in}) \quad (2.29)$$

It is easy to see that such expression can be written as

$$\frac{p_f - p_{in}}{p_f - p_c} = \frac{\Delta p_{in}}{\Delta p_i} = \frac{1 - \mu^2/\phi^2}{(R_{in}/r_{mn})^2} \quad (2.30)$$

According to the principle of maximum flow, it is possible to use Equation (2.25) for the optimum value of the discharge coefficient. Moreover, from Equation (2.6)  $r_{mn} = R_n \sqrt{1 - \phi}$  and Equation (2.30) becomes

$$\frac{\Delta p_{in}}{\Delta p_i} = \frac{2(1 - \phi)^2/(2 - \phi)}{(R_{in}/R_n)^2} \quad (2.31)$$

Since the ratio of pressure drops  $\Delta p_{in}/\Delta p_i$  must be less than 1, the latter equation is valid only for  $R_{in}/R_n > 1$ . In fact, when this condition is not met, the principle of maximum

flow rate is not applicable.

The normalization of the injector parameters simplifies its analysis, allowing to identify their relation with non dimensional parameters  $\mu$ ,  $\phi$  and  $A$ . The radii are normalized with respect to  $R_n$  and the velocities with respect to  $W_\Sigma$ . The conservation of mass flow rate gives

$$W_{in}F_{in} = \mu F_n W_\Sigma \quad (2.32)$$

and the conservation of angular momentum

$$R_{in}W_{in} = r_{mk}W_\Sigma \quad (2.33)$$

The ratio between Equations (2.32) and (2.33), dividing by  $R_n$  and rearranging leads to

$$\frac{r_{mk}}{R_n} = \mu \frac{F_n R_{in}}{F_{in} R_n} = \mu A \quad (2.34)$$

This is the normalized radius of the liquid film at the head end of the vortex chamber and it is only a function of  $\phi$  or  $A$ . In fact, substituting  $\mu$  and  $A$  from Equations (2.24) and (2.25) respectively, gives

$$\bar{r}_{mk} = \frac{r_{mk}}{R_n} = \sqrt{2(1-\phi)^2/(2-\phi)} \equiv \sqrt{a} \quad (2.35)$$

For simplicity, all the normalized quantities are denoted with a bar. With this notation Equation (2.6) results in

$$\bar{r}_{mn} = \sqrt{1-\phi} \quad (2.36)$$

Dividing Equation (2.35) by Equation (2.36) defines

$$\bar{r}_{mk}^2/\bar{r}_{mn}^2 = a/(1-\phi) = 2(1-\phi)/(2-\phi) \equiv b \quad (2.37)$$

The conservation of angular momentum with the normalized quantities results in

$\overline{W}_{un}\overline{r}_{mn} = \overline{W}_{\Sigma}\overline{r}_{mk}$ , therefore the azimuthal velocity in the nozzle is

$$\overline{W}_{un} = \overline{r}_{mk}/\overline{r}_{mn} = \sqrt{2(1-\phi)/(2-\phi)} \quad (2.38)$$

The axial velocity can be written as

$$\overline{W}_{an} = \sqrt{1 - \overline{W}_{un}^2} = \sqrt{1 - 2(1-\phi)/(2-\phi)} = \sqrt{\phi/(2-\phi)} \quad (2.39)$$

The spreading angle of the liquid sheet at the injector exit is derived with the ratio of Equations (2.38) and (2.39) as follows

$$\alpha_n = \tan^{-1}(W_{un}/W_{an}) = \tan^{-1}(\overline{W}_{un}/\overline{W}_{an}) = \tan^{-1}\sqrt{2(1-\phi)/\phi} \quad (2.40)$$

Similarly, it is possible to determine the velocities and the spreading angle downstream of

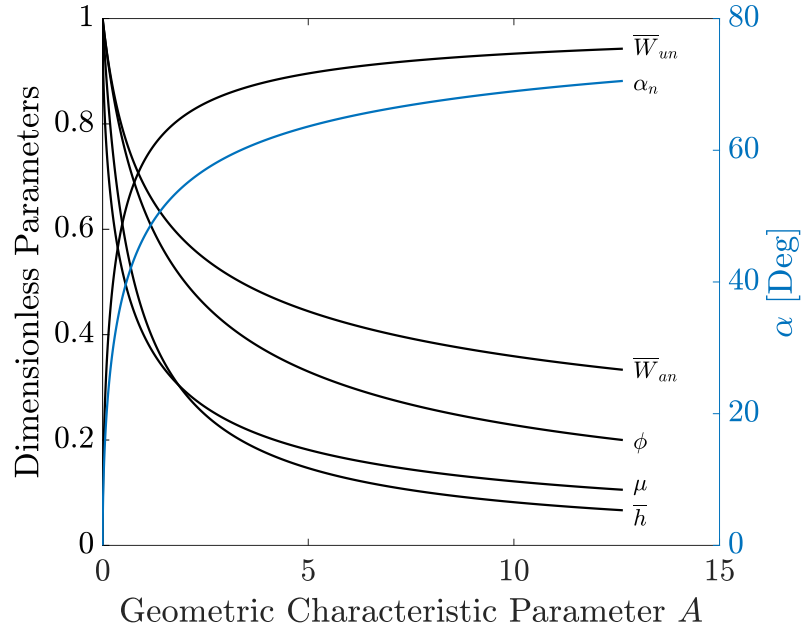


Figure 2.2: Dimensionless parameters as a function of the geometric characteristic parameter  $A$ .

the injector exit  $\alpha_e$ . The conservation of angular momentum at the exit,  $W_{ue}R_n = W_{\Sigma}r_{mk}$ ,

leads to the following expression for the azimuthal velocity

$$\overline{W}_{ue} = r_{mk}/R_n = \sqrt{2(1-\phi)^2/(2-\phi)} = \sqrt{a} \quad (2.41)$$

Consequently, the axial velocity is

$$\overline{W}_{ae} = \sqrt{1 - \overline{W}_{ue}^2} = \sqrt{1 - a} \quad (2.42)$$

From the ratio of Equations (2.41) and (2.42), the angle  $\alpha_e$  is computed as

$$\alpha_e = \tan^{-1} \sqrt{a/(1-a)} \quad (2.43)$$

Another form of Equation (2.42) is

$$W_{ae} = W_{\Sigma} \sqrt{1-a} = W_{\Sigma} \sqrt{(3-2\phi)\phi/(2-\phi)} \quad (2.44)$$

and its ratio with the axial velocity in the nozzle gives

$$\overline{W}_{ae}/\overline{W}_{an} = \sqrt{(1-a)(2-\phi)/\phi} = \sqrt{3-2\phi} \quad (2.45)$$

For a liquid film with a thickness that tends to zero,  $\phi \rightarrow 0$ , thus

$$\overline{W}_{ae} = \sqrt{3} \overline{W}_{an} \quad (2.46)$$

The dimensionless inlet velocity can be determined from Equations (2.33) and (2.35) as follows

$$\overline{W}_{in} \overline{R}_{in} = \overline{r}_{mk} \Rightarrow \overline{W}_{in} = \frac{\sqrt{a}}{\overline{R}_{in}} \quad (2.47)$$

The flow parameters in the vortex chamber can be obtained applying the condition of flow continuity. Since  $\pi(\overline{R}_n^2 - \overline{r}_{mn}^2)$  and  $\pi(\overline{R}_{vc}^2 - \overline{r}_{mv}^2)$  are the annular flow area in the nozzle

and vortex chamber respectively, the continuity condition results in

$$\overline{W}_{av} = \overline{W}_{an} \frac{\overline{R}_n^2 - \overline{r}_{mn}^2}{\overline{R}_{vc}^2 - \overline{r}_{mv}^2} \quad (2.48)$$

The latter equation can be rewritten with the aid of Equations (2.6) and (2.7) obtaining

$$\overline{W}_{av} = \overline{W}_{an} \frac{\phi}{\overline{R}_{vc}^2 - \overline{r}_{mv}^2} = \frac{\mu}{\overline{R}_{vc}^2 - \overline{r}_{mv}^2} \quad (2.49)$$

Moreover, considering that from Equation (2.1)  $W_{uv}^2 = W_{\Sigma}^2 - W_{av}^2$ , from the conservation of angular momentum  $W_{uv}r_{mv} = W_{\Sigma}r_{mk}$ , and from Equation (2.35)  $\overline{r}_{mk}^2 = a$ , it is possible to write

$$\overline{r}_{mv}^2 = \frac{a}{1 - \overline{W}_{av}^2} \quad (2.50)$$

This expression and Equation (2.49) allow to determine  $W_{av}$  and  $r_{mv}$ .

## 2.2 Linear Dynamics of Swirl Injectors

The main mission of propellant injectors is to achieve propellant atomization and the formation of a high quality combustible mixture. However, injectors are characterized by non-stationary processes and thus can be treated as a dynamic component of the engine. The oscillations generated in the feed-line due to turbulent flow and in the combustion chamber due to unsteady combustion are some of the sources of oscillations. The unsteady processes can be modified and controlled by designing an injector with specific response characteristics to disturbances in input. Following and correcting the typos in the available literature, it is possible to derive the total injector transfer function as a product of the response function of each injector part. A swirl injector can be decomposed in three main elements: tangential passages, vortex chamber and nozzle. The tangential inlets are treated as jet injectors, while the dynamics in vortex chamber and nozzle is based on the formulation of a wave equation for disturbances propagating in a liquid with centrifugal force, as it

is shown in [4].

A code was implemented to replicate the response function amplitude and phase graphs shown in [23].

### 2.2.1 Tangential Channels

Each instantaneous operating parameter can be decomposed into a mean value and a pulsation component as follows

$$\Delta\tilde{p} = \Delta p + \Delta p' \quad (2.51)$$

$$\tilde{W} = W + W' \quad (2.52)$$

where  $p$  and  $W$  are pressure and axial velocity, respectively. The one-dimension Euler equation in the axial direction for an inviscid liquid is

$$\frac{\partial\tilde{W}}{\partial t} + \tilde{W} \frac{\partial\tilde{W}}{\partial z} = -\frac{1}{\rho} \frac{\partial\tilde{p}}{\partial z} \quad (2.53)$$

In the case of a short jet injector with a length  $L_J$  much smaller than the wavelength of oscillation, the integration of Equation (2.53) in the  $z$  direction from the manifold at  $z_1 = 0$  with  $p_1 = p_f$  and  $\tilde{W}_1 = 0$ , and the exit at  $z_2 = L_J$  with  $p_2 = p_c$  and  $\tilde{W}_2 = \tilde{W}$ , gives

$$\frac{\partial\tilde{W}}{\partial t} + \frac{\tilde{W}^2}{2L_J} = \frac{\tilde{p}_f - \tilde{p}_c}{\rho L_J} \equiv \frac{\Delta\tilde{p}}{\rho L_J} \quad (2.54)$$

The substitution of Equations (2.51) and (2.52) in Equation (2.54) with the mean value  $W$  independent of time,  $\Delta p/\rho = W^2/2$  from the Bernoulli's equation and considering only first order terms, leads to the linearized equation that follows

$$\frac{\partial W'}{\partial t} + \frac{W}{L_J} W' = \frac{|\Delta p'|}{\rho L_J} e^{i\omega t} \quad (2.55)$$

where, for harmonic oscillations in time

$$\Delta p' = |\Delta p'| e^{i\omega t}, \quad W' = |W'| e^{i\omega t} \quad (2.56)$$

Keeping the latter expressions in mind, Equation (2.55) can be easily solved and the result is

$$W' = \frac{\Delta p'}{\rho W + i\omega \rho L_J} \quad (2.57)$$

Moreover, it is straight forward to derive the transfer function that relates velocity and pressure drop fluctuations normalized with respect to their mean value. In fact, rearranging Equation (2.57) and multiplying both sides by  $\Delta p/W$  with  $\Delta p/\rho = W^2/2$ , the transfer function of the jet injector is

$$\Pi_J = \frac{W'/W}{\Delta p'/\Delta p} \equiv \frac{\overline{W}'_J}{\Delta \overline{p}'_J} = \frac{\Delta p}{W} \frac{1}{\rho W + i\omega \rho L_J} = \frac{1}{2} \frac{1 - \frac{i\omega L_J}{W}}{1 + \left(\frac{\omega L_J}{W}\right)^2} = \frac{1}{2} \frac{1 - iSh_J}{1 + Sh_J^2} \quad (2.58)$$

where the Strouhal number is  $Sh_J = \omega L_J/W$ . The real and imaginary part are

$$Re \Pi_J = \frac{1}{2} \frac{1}{1 + Sh_J^2}, \quad Im \Pi_J = -\frac{1}{2} \frac{Sh_J}{1 + Sh_J^2} \quad (2.59)$$

Consequently, the phase angle  $\Phi_J$  between  $\overline{W}'_J$  and  $\Delta \overline{p}'_J$  is

$$\Phi_J = \arctan \frac{Im \Pi_J}{Re \Pi_J} = -\arctan Sh_J \quad (2.60)$$

The plot of the amplitude-phase diagram of the transfer function is depicted in Figure 2.3, where  $\Delta \overline{p}' = 1$  arbitrarily. It is possible to state that for short injectors the amplitude of the pulsation  $W'$  decreases as  $Sh$  increases, while  $\Phi_J$  tends asymptotically to  $\pi/2$ .

The analysis for jet injectors can be directly applied to the tangential channels if their length is much smaller than the wavelength of oscillation.

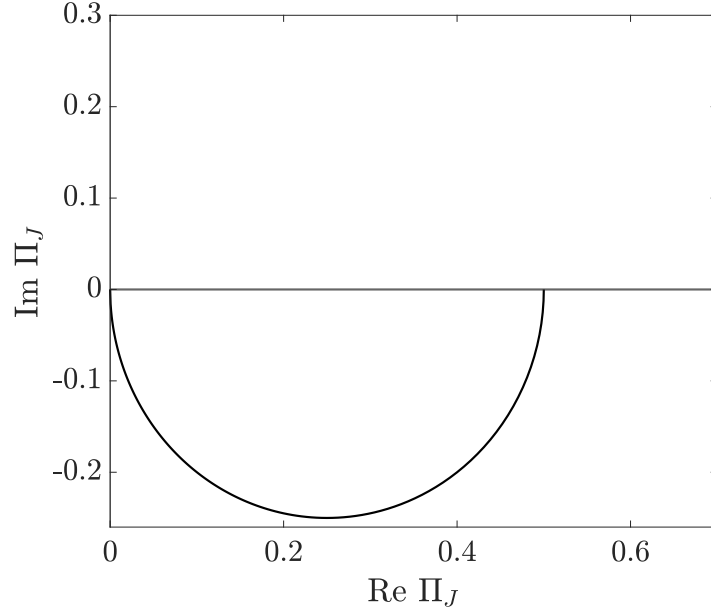


Figure 2.3: Transfer function diagram for short jet injectors.

### 2.2.2 Swirling Chamber

#### *Wave Equation and Wave Speed*

The analysis of the swirling flow in the vortex chamber and nozzle requires the derivation of the wave equation that governs the disturbance propagation in the swirling liquid. The final expression can be obtained following the approach presented in [44].

For an inviscid axisymmetric flow in the  $z$  direction, the Euler equations are

$$\frac{d\tilde{W}_r}{dt} = \frac{W_u^2}{r} - \frac{1}{\rho} \frac{\partial \tilde{p}}{\partial r} \quad (2.61)$$

$$\frac{d\tilde{W}_a}{dt} = -\frac{1}{\rho} \frac{\partial \tilde{p}}{\partial z} \quad (2.62)$$

In addition to the assumption of inviscid fluid, the following assumptions are applied:

- the radial acceleration is considered negligible  $dW_r/dt \approx 0$
- the amplitude of oscillations are small compared to the gas core radius  $\xi \ll r_m$

- the axial velocity component  $W_a$  is uniform in the thin liquid film at any cross section along the symmetry axis.

Therefore, Equation (2.61) becomes

$$\frac{\partial \tilde{p}}{\partial r} = \rho \frac{W_u^2}{r} \quad (2.63)$$

Using Equation (2.17) and integrating from the free liquid surface where  $r = r_m + \xi$  and  $p = p_c$  to a radius  $r$  in the liquid film, the following expression can be written

$$\tilde{p} - p_c = \rho \int_{r_m + \xi}^r \frac{W_{in}^2 R_{in}^2}{r^3} dr = \frac{\rho}{2} W_{in}^2 R_{in}^2 \left[ \frac{1}{(r_m + \xi)^2} - \frac{1}{r^2} \right] \quad (2.64)$$

The differentiation of this equation along  $z$  leads to

$$\frac{\partial \tilde{p}}{\partial z} = -\rho \frac{W_{in}^2 R_{in}^2}{(r_m + \xi)^3} \frac{\partial \xi}{\partial z} \quad (2.65)$$

The substitution of Equation (2.65) into Equation (2.62) neglecting the convective part of the material derivative as in [44, 45], and recalling  $\xi \ll r_m$  gives

$$\frac{d\tilde{W}_a}{dt} \approx \frac{\partial \tilde{W}_a}{\partial t} = \frac{W_{in}^2 R_{in}^2}{r_m^3} \frac{\partial \xi}{\partial z} \quad (2.66)$$

The additional equation required to obtain the wave equation can be derived applying the conservation of mass. Any cross section in the vortex chamber is characterized by a gas core and a liquid ring. Considering two cross sections at a distance  $dz$ , the volume of liquid that passes through each one of them in a time  $dt$  is

$$\left[ \tilde{W}_a \pi (R_{vc}^2 - (r_m + \xi)^2) \right]_z dt, \quad \left[ \tilde{W}_a \pi (R_{vc}^2 - (r_m + \xi)^2) \right]_{z+dz} dt \quad (2.67)$$

Therefore, the change in volume in  $dt$  between the cross sections is

$$\frac{\partial \left[ \tilde{W}_a \pi (R_{vc}^2 - (r_m + \xi)^2) \right]}{\partial z} dz dt \quad (2.68)$$

Due to incompressibility of the liquid, a change in volume corresponds to a change in the level of the fluid. The latter changes by a quantity  $(\partial \xi / \partial t) dt$  in an interval  $dt$ , thus the change in volume is

$$2\pi r_m \frac{\partial \xi}{\partial t} dz dt \quad (2.69)$$

Equations (2.68) and (2.69) must be equal, leading to

$$\frac{\partial \xi}{\partial t} = \frac{R_{vc}^2 - (r_m + \xi)^2}{2r_m} \frac{\partial \tilde{W}_a}{\partial z} - \frac{r_m + \xi}{r_m} \tilde{W}_a \frac{\partial \xi}{\partial z} \quad (2.70)$$

Recalling that  $\xi$  is small and neglecting the last term since it is second order [44, 45]

Equation (2.70) can be simplified:

$$\frac{\partial \xi}{\partial t} = \frac{R_{vc}^2 - r_m^2}{2r_m} \frac{\partial \tilde{W}_a}{\partial z} \quad (2.71)$$

The differentiation of Equations (2.66) and (2.71) with respect to space  $z$  and time  $t$ , respectively, and the subsequent elimination of the mixed derivatives that appear in both expressions, give

$$\frac{\partial^2 \xi}{\partial t^2} = \frac{W_{in}^2 R_{in}^2}{r_m^3} \frac{R_{vc}^2 - r_m^2}{2r_m} \frac{\partial^2 \xi}{\partial z^2} \quad (2.72)$$

This expression is the wave equation that describes the propagation of disturbances on the liquid surface in the axial direction. It is easy to note that Equation (2.72) has the following form

$$\frac{\partial^2 \xi}{\partial t^2} = W_w^2 \frac{\partial^2 \xi}{\partial z^2} \quad (2.73)$$

where  $W_w$  is the surface wave propagation speed, which explicitly is

$$W_w = \sqrt{\frac{W_{in}^2 R_{in}^2}{r_m^3} \frac{R_{vc}^2 - r_m^2}{2r_m}} = \frac{W_{in} R_{in}}{r_m^2} \sqrt{\frac{R_{vc}^2 - r_m^2}{2}} \quad (2.74)$$

Analyzing this expression, it is possible to notice the analogy with the propagation speed of shallow-water waves  $W_{sh}$ , which is

$$W_{sh} = \sqrt{g_{sh} h_{sh}} \quad (2.75)$$

where  $g_{sh} = (W_{in}^2 R_{in}^2)/(r_m^3)$  corresponds to the centrifugal acceleration and  $h_{sh} = (R_{vc}^2 - r_m^2)/(2r_m)$  corresponds to an effective thickness of the liquid film. In shallow-water waves under the effect of gravitational force,  $g_{sh}$  is the gravitational acceleration and  $h_{sh}$  the water depth. From Equation (2.66) it is possible to write

$$\frac{\partial W'_a}{\partial t} = \frac{W_{in}^2 R_{in}^2}{r_m^3} \frac{\partial \xi}{\partial z} \quad (2.76)$$

An expression for  $\xi$  is given by the solution of Equation (2.72) for a semi-infinite vortex chamber, which is the following

$$\xi = \Omega e^{i\omega(t-z/W_w)} \quad (2.77)$$

The latter form for  $\xi$  can be substituted in Equation (2.76) and expanding  $W'_a = |W'_a| e^{i\omega(t-z/W_w)}$ , the amplitude of the axial velocity oscillation is

$$|W'_a| = \frac{\Omega W_{in}^2 R_{in}^2}{W_w r_m^3} \quad (2.78)$$

### Wave Amplitude

The wave speed of Equation (2.74) can be rewritten in a non-dimensional form through the angular momentum conservation  $W_{in}R_{in} = W_{\Sigma} r_{mk}$ , with  $r_m = r_{mk}$ , and  $\bar{r}_{mk} = \sqrt{a}$

$$\bar{W}_w = \frac{W_w}{W_{\Sigma}} = \frac{W_{\Sigma} r_{mk}}{r_{mk}^2} \sqrt{\frac{R_{vc}^2 - r_{mk}^2}{2}} = \sqrt{\frac{1}{2} \left( \frac{\bar{R}_{vc}^2}{a} - 1 \right)} \quad (2.79)$$

Moreover, the liquid axial velocity in the vortex chamber is given by Equation (2.49), therefore the total velocity of a surface wave propagating in the vortex chamber is

$$\bar{W}_{w,vc} = \bar{W}_w + \bar{W}_{av} = \sqrt{\frac{1}{2} \left( \frac{\bar{R}_{vc}^2}{a} - 1 \right)} + \frac{\mu}{\bar{R}_{vc}^2 - a} \quad (2.80)$$

The surface wave amplitude as a function of the inlet velocity fluctuation  $W'_{in}$  is derived from considerations on the volume flow rate. The total instantaneous volume flow rate can be expressed as

$$Q + Q' = \int_{r_m - \xi}^{R_{vc}} 2\pi(W_{av} + W'_{av})rdr \quad (2.81)$$

where

$$\begin{aligned} \int_{r_m - \xi}^{R_{vc}} 2\pi W_{av} r dr &= Q + \int_{r_m - \xi}^{r_m} 2\pi W_{av} r dr = Q + 2\pi W_{av} r_m \xi \\ \int_{r_m - \xi}^{R_{vc}} 2\pi W'_{av} r dr &= \int_{r_m - \xi}^{r_m} 2\pi W'_{av} r dr + \int_{r_m}^{R_{vc}} 2\pi W'_{av} r dr = 2\pi W'_{av} r_m \xi + \pi W'_{av} (R_{vc}^2 - r_m^2) \end{aligned} \quad (2.82)$$

The second order term in the last expression of Equation (2.82) can be neglected. After summing the two right hand sides of Equation (2.82) and comparing to Equation (2.81), the fluctuating volume flow rate is given by

$$Q' = 2\pi W_{av} r_m \xi + \pi W'_{av} (R_{vc}^2 - r_m^2) \quad (2.83)$$

Substituting Equation (2.78) and  $W_{av} = W_{\Sigma} \bar{W}_{av}$  from Equation (2.80) into Equation (2.83), the following expression is obtained

$$Q' = 2\pi \frac{W_{\Sigma} \mu}{R_{vc}^2 - a} r_{mk} \Omega_{vL} + \pi \Omega_{vL} \frac{W_{in}^2 R_{in}^2}{W_{w,vc} r_{mk}^3} (R_{vc}^2 - r_{mk}^2) \quad (2.84)$$

The second term corresponds to volume flow rate fluctuations at the head end of the injector where  $W_{av} = 0$  and it can be rewritten as

$$Q'_k = \frac{\pi \bar{\Omega}_{vL,k} W_{\Sigma} R_n^2 (\bar{R}_{vc}^2 - a)}{\bar{W}_{w,vc}} \quad (2.85)$$

with  $\bar{\Omega}_{vL} = \Omega_{vL}/r_{mk}$ . Equating  $Q'_k$  to the volume flow rate oscillation through the tangential inlets  $Q'_{in} = F_{in} W'_{in}$  for continuity of the liquid flow, the wave amplitude  $\bar{\Omega}_{vL}$  results in

$$\bar{\Omega}_{vL,k} = \frac{1}{A \sqrt{2(\bar{R}_{vc}^2 - a)}} \left| \frac{W'_{in}}{W_{in}} \right| \quad (2.86)$$

where the geometric parameter  $A = \bar{R}_{in} F_n / F_{in}$  was used and  $W_{w,vc} = W_w$  at the head-end. Note that  $\Omega_{vL,k}$  is the wave amplitude at the head-end where the liquid axial velocity is zero, while  $\Omega_{vL}$  accounts for  $W_{av}$ . The amplitude  $\Omega_{vL}$  can be obtained from Equation (2.84). The latter can be rewritten using Equation (2.85) and with the approximation that  $W_{w,vc} = W_w$  as follows

$$Q' = \pi R_n^2 \bar{\Omega}_{vL} W_{\Sigma} \left( \sqrt{2a(\bar{R}_{vc}^2 - a)} + \frac{2\mu a}{\bar{R}_{vc}^2 - a} \right) \quad (2.87)$$

It is now possible to obtain  $\bar{\Omega}_{vL}$  equating  $Q'$  and  $Q'_{in}$

$$\bar{\Omega}_{vL} = \frac{W'_{in} \bar{R}_{in}}{A W_{\Sigma} \left( \sqrt{2a(\bar{R}_{vc}^2 - a)} + \frac{2\mu a}{\bar{R}_{vc}^2 - a} \right)} \quad (2.88)$$

Finally, Equation (2.88) can be divided by Equation (2.86) to get the following expression

$$\frac{\bar{\Omega}_{vL}}{\bar{\Omega}_{vL,k}} = \frac{\sqrt{(\bar{R}_{vc}^2 - a)^3}}{\sqrt{(\bar{R}_{vc}^2 - a)^3 + \mu\sqrt{2a}}} \quad (2.89)$$

### 2.2.3 Transfer Function of Open-End Injectors

Following the approach used by Bazarov [5] for closed-end injectors, L. Yang [26] derived an analytical expression for the transfer function of an open-end swirl injector. The absence of a conical converging section allows the disturbance waves to travel from the head-end to the exit of the injector without reflecting back. Therefore, there is no superposition of forward and backward traveling waves in the vortex chamber. Moreover, the axial velocity of the liquid flow in open injectors is higher than in closed injectors and its effect cannot be neglected. Even in the case of open injectors the total transfer function is the product of the response functions of the different parts of the injector.

In Section 2.2.1, the response function for tangential inlets  $\Pi_J$  was derived. This function establishes a connection between non-dimensional volume flow rate pulsations and pressure drop fluctuations across the inlet channels. With a slight change of notation in the subscript  $\Pi_J$  is the following

$$\Pi_J = \Pi_T = \frac{W'_T/W_T}{\Delta p'_T/\Delta p_T} \equiv \frac{\bar{W}'_T}{\Delta \bar{p}'_T} \quad (2.90)$$

where the subscript  $T$  substitutes  $J$  and is used equivalently to  $in$  to indicate the tangential inlets.

The dynamics of the vortex chamber has a higher complexity. The mass flow rate fluctuations induced by pressure drop fluctuations across the inlet channels generate two types of waves. Firstly, surface waves that propagate axially towards the exit of the injector are indicated with subscript  $II$ . Secondly, vorticity waves which travel radially and are associated to pulsations of the circumferential velocity at different radii. Vorticity waves

are indicated by subscript *III*. It is assumed that the pressure drop fluctuation in the vortex chamber is equally shared by the two types of waves, therefore

$$\Delta \bar{p}'_{vc} = \Delta \bar{p}'_{vc,II} + \Delta \bar{p}'_{vc,III} \quad (2.91)$$

and the total pressure drop is

$$\Delta \bar{p}'_i = \Delta \bar{p}'_{vc} + \Delta \bar{p}'_T \quad (2.92)$$

The expression for a surface wave at the head-end of the injector is given by

$$\xi_k = \Omega_{vL} e^{i\omega t} \quad (2.93)$$

When the wave travels axially a distance  $L_{vc}$  until the exit of the injector, its amplitude will be damped by a factor  $e^{-\nu\Phi_{vc}}$  and its phase shifted by an angle  $\Phi_{vc}$

$$\xi_{vn} = \Omega_{vL} e^{i(\omega t - \Phi_{vc}) - \nu\Phi_{vc}} \quad (2.94)$$

where  $\Phi_{vc} = \omega t_{vc} = \omega L_{vc}/W_{w,vc}$  and  $\nu$  is a dimensionless parameter to account for viscous friction. Such parameter is determined experimentally for various fluids.

Bazarov [5] shows that for a long vortex chamber, which is the case of an open injector, it is possible to write

$$K_{\Sigma,II} = \frac{\Delta p'_{vcII}/\Delta p_T}{2W'_{in}/W_{in}} = \frac{\bar{\Omega}_{vL}}{W'_{in}/W_{in}} \quad (2.95)$$

It should be noted that  $W'_{in}/W_{in} = Q'_T/Q_T$  and  $\bar{\Omega}_{vL}$  is derived from Equation (2.89).

Therefore, the transfer function for surface waves at the head-end of the injector is

$$\Pi_{vcII} = \frac{\Delta p'_{vcII}/\Delta p_T}{2Q'_T/Q_T} = K_{\Sigma,II} \quad (2.96)$$

As a consequence, at the exit of the injector

$$\Pi_{vn} = K_{\Sigma,II} e^{-i\Phi_{vc} - \nu\Phi_{vc}/2\pi} = \frac{Q'_{vn}/Q_{vn}}{Q'_T/Q_T} \quad (2.97)$$

The last term needed for the total transfer function is the response function associated to vorticity waves derived by Bazarov [5]

$$\Pi_{vcIII} = \frac{\Delta p'_{vcIII}/\Delta p_T}{2Q'_T/Q_T} = \frac{\bar{R}_{vc} - \sqrt{a}}{\bar{R}_{vc}} \int_0^1 e^{i(\omega t - f(\bar{x}))} e^{-\nu f(\bar{x})} \frac{d\bar{x}}{\left[1 - \frac{\bar{R}_{vc} - \sqrt{a}}{\bar{R}_{vc}} \bar{x}\right]^3} \quad (2.98)$$

where

$$f(\bar{x}) = \frac{\omega R_{in} \bar{R}_{vc}^2 - a}{W_{\Sigma} \mu} \bar{x} \tan\left(\frac{\pi \bar{x}}{2}\right) \quad (2.99)$$

At this point, the total transfer function can be constructed through the following procedure. Let's divide Equation (2.92) by  $\Delta p_T$  to obtain

$$\frac{\Delta p'_i}{\Delta p_T} = \frac{\Delta p'_{vc}}{\Delta p_T} + \frac{\Delta p'_T}{\Delta p_T} = \left[2(\Pi_{vcII} + \Pi_{vcIII}) + \frac{1}{\Pi_T}\right] \frac{Q'_T}{Q_T} \quad (2.100)$$

and using  $\Delta p_T/\Delta p_i = a/\bar{R}_{in}^2$  Equation (2.100) becomes

$$\frac{\Delta p'_i}{\Delta p_i} = \frac{a}{\bar{R}_{in}^2} \left[ \frac{2\Pi_T(\Pi_{vcII} + \Pi_{vcIII}) + 1}{\Pi_T} \right] \frac{Q'_T}{Q_T} \quad (2.101)$$

Using Equation (2.97), the volume flow rate pulsation near the exit of the injector can be related to the total pressure drop fluctuation as follows

$$\frac{\Delta p'_i}{\Delta p_i} = \frac{a}{\bar{R}_{in}^2} \left[ \frac{2\Pi_T(\Pi_{vcII} + \Pi_{vcIII}) + 1}{\Pi_T \Pi_{vn}} \right] \frac{Q'_{vn}}{Q_T} \quad (2.102)$$

In conclusion, the total injector transfer function is

$$\Pi_i = \frac{Q'_{vn}/Q_{vn}}{\Delta p'_i/\Delta p_i} = \frac{\bar{R}_{in}^2}{a} \left[ \frac{\Pi_T \Pi_{vn}}{2\Pi_T(\Pi_{vcII} + \Pi_{vcIII}) + 1} \right] \quad (2.103)$$

where the conservation of mass flow rate was used, in fact  $Q_T = Q_{vc} = Q_{vn}$ .

The injector response function  $\Pi_i$  was plotted by Fu et al. in [23] varying several parameters. The results are shown in Figures 2.4 and 2.5 alongside the graphs obtained through a MATLAB code to replicate the analytical expression of Equation 2.103. Both the code and Fu et al. use the approximation  $R_{in} \approx R_{vc}$ . The comparison shows that the MATLAB code replicates perfectly the results obtained by Fu et al and this validates the code.

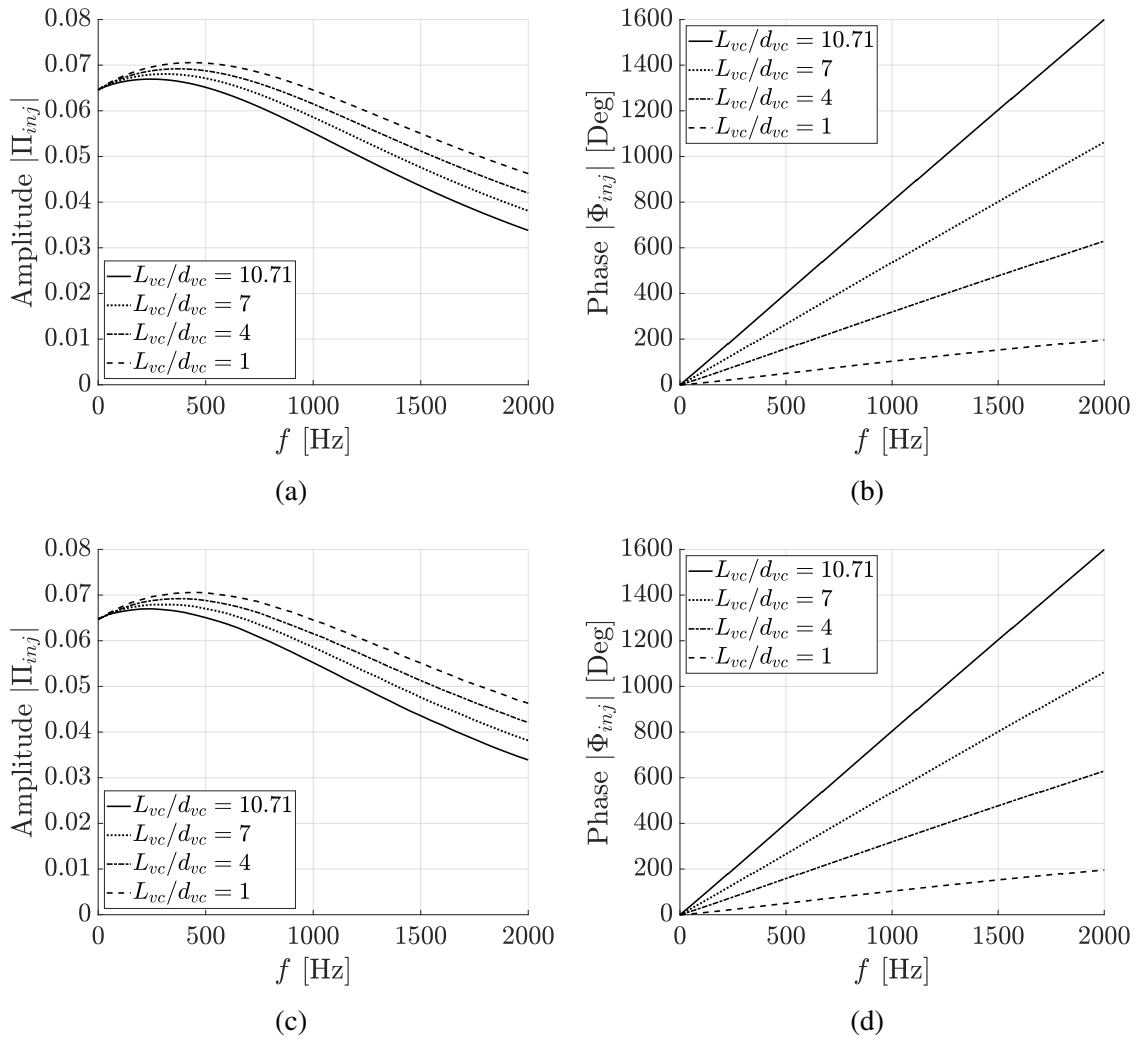
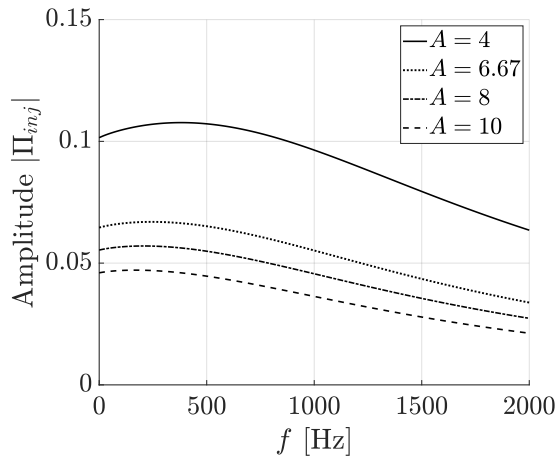
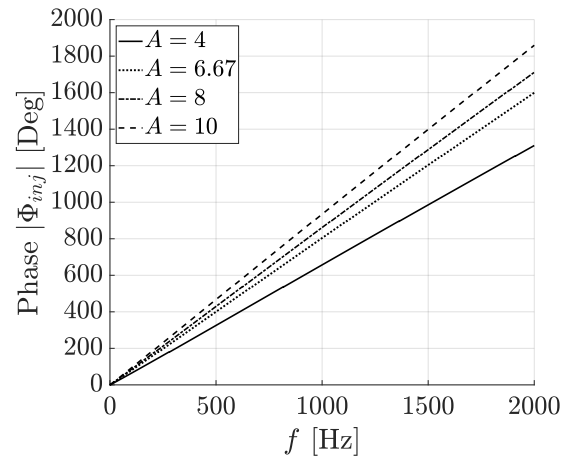


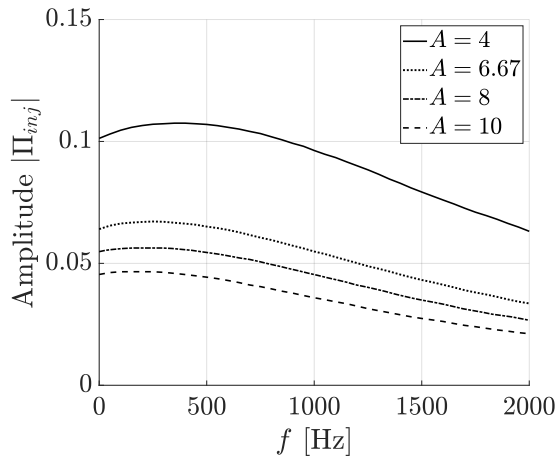
Figure 2.4: Theoretical Validation – Amplitude and phase diagrams of the injector transfer function as a function of frequency for different values of injector length to diameter ratio  $L_{vc}/d_{vc}$ . Graphs (a) and (b) are obtained through a MATLAB code, (c) and (d) are from [23].



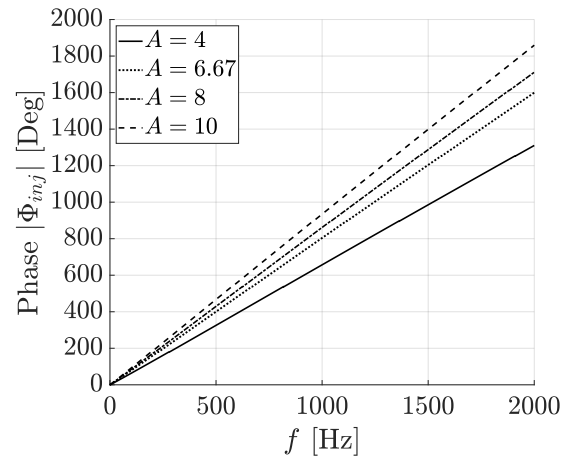
(a)



(b)



(c)



(d)

Figure 2.5: Theoretical Validation – Amplitude and phase diagrams of the injector transfer function as a function of frequency for different values of the geometric characteristic parameter  $A$ . Graphs (a) and (b) are obtained through a MATLAB code, (c) and (d) are from [23].

## CHAPTER 3

### TRANSFER FUNCTION OF OPEN-HEAD OPEN-END INJECTORS

The classical theory of liquid swirl injectors relies on the assumption of inviscid fluid, introducing viscous effects through an empirically determined artificial damping factor, denoted as  $\nu$  [4]. The classical theory considers a stationary gas core surrounded by a swirling liquid and, therefore, it cannot be automatically generalized to an OHOE swirl injector with coaxial gas flow. As an initial approximation, it is reasonable to assume that the steady-state theory of closed-head injectors remains applicable for OHOE injectors in describing the swirling liquid. Consequently, the conserved quantities and dimensionless parameters align with those outlined in classical theory. It is assumed, in fact, that the liquid flow is purely swirling where the tangential inlets are located. This is a strong but plausible assumption if the liquid-to-air Momentum Flux Ratio (MFR) defined as  $\rho_l W_l^2 / \rho_g W_g^2$  is high. For instance, considering air at 100 – 150 m/s [46, 47] and water injected through the tangential channels at 20 – 50 m/s, the MFR is of the order of 20 – 250. As a consequence, the high liquid momentum flux in the tangential direction with respect to the gas momentum flux in the axial direction may cause some liquid to move upstream towards the gas inlet. However, after a transient, the liquid film is expected reach equilibrium in the axial direction due to the presence of strong aerodynamic forces caused by high speed gas. This condition is depicted schematically in Figure 3.1, but it is necessary to confirm this assumption through CFD simulations.

In this section, an extension of the classical theory is introduced to incorporate the relevant physical phenomena in OHOE injectors. Initially, a forced wave equation is derived, considering shear stress at the liquid-wall and liquid-gas interfaces. Subsequently, the injector transfer function is adjusted to include analytical damping factors, eliminating the need for any artificial factors.

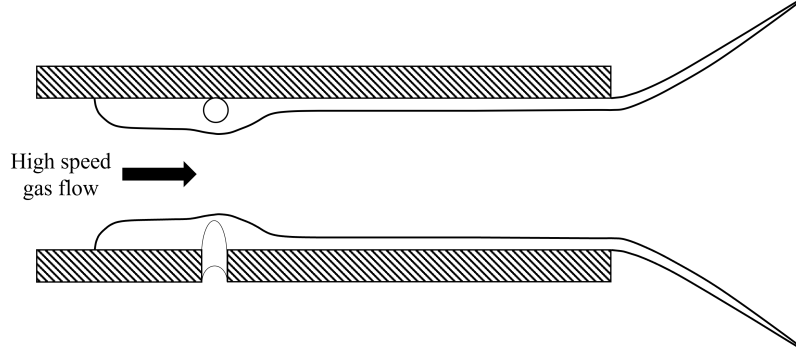


Figure 3.1: Schematic representation of OHOE injector at steady-state.

### 3.1 Forced Wave Equation

The extension of the classical theory incorporates viscous effects into the equation of motion for the swirling liquid by accounting for shear stress interactions between the liquid and the wall, as well as between the liquid and the gas. Shear stress at the liquid-wall interface can be modelled as follows

$$\tau_{lw} = -\frac{\rho_l C_{f,lw}}{2} \tilde{W}_{av}^2 \quad (3.1)$$

where  $C_{f,lw}$  is the liquid-wall friction factor,  $\rho_l$  is the liquid density and  $\tilde{W}_{av} = W_{av} + W'_{av}$  is the instantaneous liquid velocity in the axial direction. At the liquid-gas interface, shear stress depends on the relative velocity between the gas and the liquid flows:

$$\tau_{lg} = \frac{\rho_g C_{f,lg}}{2} (\tilde{W}_{av} - W_g)^2 \quad (3.2)$$

where the gas velocity  $W_g$  is assumed to be equal to its steady-state value. A schematic representation of the shear stress acting on the fluid is shown in (Figure 3.2).

The equation of motion in the classical theory, Equation 2.66, can be modified to include shear stress in the radial direction:

$$\frac{\partial W'_{av}}{\partial t} = C \frac{\partial \xi}{\partial z} + \frac{1}{\rho_l} \frac{\partial \tau}{\partial r} \quad (3.3)$$

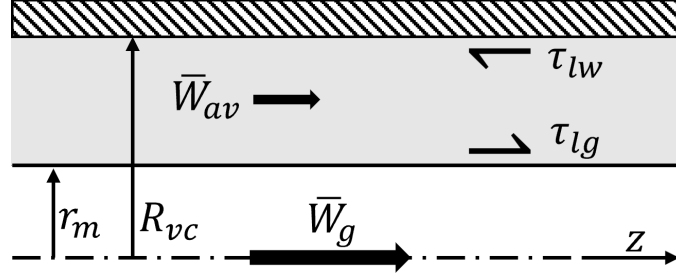


Figure 3.2: Illustration of the shear stress acting on the liquid film in the axial direction.

where  $C = W_{in}^2 R_{in}^2 / r_m^3$ . Assuming that the pulsation in the axial velocity is constant in the radial direction, it is possible to integrate the previous equation. This allows to distribute the shear stress at the two interfaces along the thickness of the liquid film. The integration of the equation of motion leads to

$$\begin{aligned} \frac{\partial W'_{av}}{\partial t} &= C \frac{\partial \xi}{\partial z} + \frac{\tau_{lw} - \tau_{lg}}{\rho_L (R_{vc} - (r_m + \xi))} \\ &= C \frac{\partial \xi}{\partial z} + \frac{1}{(R_{vc} - (r_m + \xi))} \left[ -\frac{C_{f,lw}}{2} \tilde{W}_{av}^2 - \frac{\rho_g C_{f,lg}}{\rho_l} \frac{1}{2} (\tilde{W}_{av} - W_g)^2 \right] \end{aligned} \quad (3.4)$$

Neglecting  $\xi$  with respect to  $r_m$ , differentiating Equation 3.4 along  $z$ , and linearizing the stress terms leads to

$$\frac{\partial^2 W'_{av}}{\partial t \partial z} = C \frac{\partial^2 \xi}{\partial z^2} - \frac{1}{(R_{vc} - r_m)} \left[ C_{f,lw} \bar{W}_{av} + \frac{\rho_g}{\rho_l} C_{f,lg} (\bar{W}_{av} - W_g) \right] \frac{\partial W'_{av}}{\partial z} \quad (3.5)$$

From the conservation of mass described by Equation 2.71 it is possible to substitute  $\partial W'_{av} / \partial z$  in Equation 3.5. Subsequently, the obtained equation can be used to substitute the mixed derivative in time and space that appears in the mass equation differentiated in time. This procedure leads to the forced wave equation that follows

$$\frac{\partial^2 \xi}{\partial t^2} + B \frac{\partial \xi}{\partial t} = W_w^2 \frac{\partial^2 \xi}{\partial z^2} \quad (3.6)$$

where  $B = \left[ C_{f,lw} \bar{W}_{av} + \frac{\rho_g}{\rho_l} C_{f,lg} (\bar{W}_{av} - W_g) \right] / (R_{vc} - r_m)$ . As a first approximation, the

models used for the friction factors are

$$C_{f,lw} = 0.0791(Re_l)^{-1/4} \quad \text{Blasius (1913)} \quad (3.7)$$

with  $Re_L = \overline{W}_{av} 2R_{vc} / \nu_l$  for turbulent flow in a pipe, and

$$\begin{aligned} C_{f,lg} &= 0.00355/4 \quad Re_g < 9000 \\ C_{f,lg} &= 2.82(Re_g)^{-0.522} \quad Re_g > 9000 \end{aligned} \quad (3.8)$$

with  $Re_g = W_g 2r_m / \nu_g$ . The last two expressions were determined using CFD simulations in a horizontal stratified two-phase flow in [48]. Although these friction factors represent a good initial guess, the flow physics involved in OHOE injectors is far from the flow structure where  $C_{f,lw}$  and  $C_{f,lg}$  of Equations (3.7) and (3.8) can be accurately employed. Therefore, it is fundamental to consider their improvement and tuning through CFD simulations or experiments for different Reynolds numbers and disturbance frequencies.

Observing the forced wave equation (Equation 3.6) derived above, it is clear how the introduction of shear stress at the liquid-wall and gas-liquid interfaces leads to the presence of the  $B$  term. Let the axial gas velocity be zero to describe a stationary gas core as in the closed-head injectors, then the contribution of the wall and the gas friction on the liquid film add up, as they are both opposite to the mean liquid flow. Conversely, for a gas velocity  $W_g > \overline{W}_{av}$  the aerodynamic forces are opposite to the wall friction effect. The gas velocity needed to overcome the wall friction is given by the following expression

$$W_g^* > \left(1 + \frac{\rho_l C_{f,lw}}{\rho_g C_{f,lg}}\right) \overline{W}_{av} \quad (3.9)$$

### 3.2 Wave Equation Solution and Injector Transfer Function

The solution of the forced wave equation has the same form as that of the standard wave equation, which is the following

$$\xi = \Omega e^{i(\omega t - kz)} \quad (3.10)$$

In this case, however, the wave number is found to be complex with the following form  $k = k_r + ik_i$ . From the substitution of Equation 3.10 into Equation 3.6 the real and imaginary parts of the wave number are

$$k_r = \frac{k_I}{\sqrt{2}} \left[ 1 + \sqrt{1 + \left( \frac{B}{\omega} \right)^2} \right]^{1/2} \quad (3.11)$$

and

$$k_i = -\frac{k_I}{\sqrt{2}} \left[ \sqrt{1 + \left( \frac{B}{\omega} \right)^2} - 1 \right]^{1/2} \quad (3.12)$$

where  $k_I = \omega/W_w$  is the wave number in the inviscid case. The angular frequency  $\omega$  is a real quantity, since the disturbances are assumed to not increase nor decay in time. Consequently, the form of the solution and wave number clearly show the presence of a spatial damping along the axial coordinate  $z$ . The wave amplitude as a function of the tangential inlet velocity pulsation is necessary to derive the new amplitude of the axial velocity pulsation. This can be done by integrating the mass equation in  $dz$

$$W'_{av} = \frac{2r_m}{R_{vc}^2 - r_m^2} \int \frac{\partial \xi}{\partial t} dz \quad (3.13)$$

and the amplitude results in the following expression

$$|W'_{av}| = \frac{2r_m}{R_{vc}^2 - r_m^2} \frac{\omega \Omega e^{k_i z}}{\sqrt{k_r^2 + k_i^2}} \quad (3.14)$$

Differently from the classical theory, the axial velocity amplitude is function of the frequency and is damped for  $z > 0$ . Substituting the previous expression in Equation 2.83, the volume flow rate pulsation is

$$Q' = \left[ 2\pi r_{mk}^2 \left( \frac{W_{\Sigma}\mu}{R_{vc}^2 - a} + \frac{\omega e^{k_i z}}{\sqrt{k_r^2 + k_i^2}} \right) \right] \bar{\Omega} = D \bar{\Omega} \quad (3.15)$$

with  $\bar{\Omega} = \Omega/r_{mk}$  and the term in brackets is  $D$  for simplicity. From the comparison with  $Q' = F_{in}|W'_{in}|$  for volume flow rate conservation, the following expression is obtained

$$K_{\Sigma,new} = \frac{\bar{\Omega}}{W'_{in}/W_{in}} = \frac{n\pi r_{in}^2 W_{in}}{D} \quad (3.16)$$

where  $F_{in} = n\pi r_{in}^2$  is the total inlet area. The parameter  $K_{\Sigma,new}$  substitutes  $K_{\Sigma,II}$  in the expressions of the transfer functions described in the classical theory. At the head-end of the injector the surface wave is determined by

$$\xi_k = \Omega e^{i\omega t} \quad (3.17)$$

Thanks to this theoretical extension, there is no necessity to introduce an artificial damping factor for the wave reaching the injector exit. In fact, the complex nature of the wave number  $k$  already includes the damping due to viscous effects. Therefore, the wave at the injector exit is

$$\xi_{vn} = \Omega e^{i(\omega t - kL_{vc})} = \Omega e^{k_i L_{vc}} e^{i(\omega t - k_r L_{vc})} \quad (3.18)$$

As a consequence, the transfer functions are modified as follows

$$\Pi_{vcII,new} = K_{\Sigma,new,0} \quad (3.19)$$

which is evaluated at  $z = 0$ , and

$$\Pi_{vn,new} = K_{\Sigma,new,L_{vc}} e^{-ik_r L_{vc} + k_i L_{vc}} \quad (3.20)$$

where  $K_{\Sigma,new,L_{vc}}$  is evaluated at  $z = L_{vc}$ . The last term to be modified is  $\Pi_{vcIII}$  since it contains a damping factor expressed as  $e^{-\nu f(\bar{x})}$ . However, as it is shown in Section 3.3, the damping coefficient has a negligible effect on the overall transfer function and it can be discarded. Thus,  $\Pi_{vcIII}$  remains unchanged.

An additional quantity of interest is the wave amplitude when the contribution of the mean axial liquid velocity is negligible or zero. This occurs at the head-end of closed-head open-end injectors and in the entire swirling chamber of closed-head closed-end injectors. Starting from Equation 2.83, setting  $W_{av} = 0$  and using Equation 3.14, the volumetric flow rate is

$$Q'_k = 2\pi r_{mk} \frac{\omega e^{k_i z}}{\sqrt{k_r^2 + k_i^2}} = 2\pi r_{mk} \frac{\Omega_k W_w}{\left[1 + \left(\frac{B}{\omega}\right)^2\right]^{1/4}} \quad (3.21)$$

The above expression must be equal to the inlet volumetric flow rate pulsation and using the definition of the geometric parameter  $A$ , the non dimensional quantities  $\bar{W}_w$  and  $\bar{r}_{mk}$ , and the conservation of angular momentum at the head-end, the following expression is found

$$\bar{\Omega}_k = \frac{F_{in} |W'_{in}| \left[1 + \left(\frac{B}{\omega}\right)^2\right]^{1/4}}{2\pi r_{mk}^2 W_w} = \frac{\left[1 + \left(\frac{B}{\omega}\right)^2\right]^{1/4}}{2A \bar{W}_w \sqrt{a}} \frac{|W'_{in}|}{W_{in}} \quad (3.22)$$

As it can be seen from this expression, the wave amplitude tends to infinity as  $\omega$  goes to zero since the other quantities are finite values. This behavior can be associated with the simplified linear approach that is used in this theoretical derivation and with the assumptions made for the tangential channels dynamics. In fact, for a constant pressure disturbance, i.e.  $\omega = 0$ , the pulsation  $|W'_{in}|$  is finite and non zero.

It was shown that the introduction of the shear stress in the equation of motion leads to the appearance of  $B$  in the wave equation. It is important to highlight that this is an

extension of the classical theory, and it is easy to verify that setting  $B$  equal to zero the previous model is recovered. In particular, with  $B = 0$

$$k_r = k_I; \quad k_i = 0 \quad (3.23)$$

which implies that the expression for the velocity pulsation amplitude  $W'_{av}$  returns to be Equation 2.78, and consequently the wave amplitude  $\Omega$ . Naturally, this becomes a fully inviscid theory and it is necessary to introduce an artificial factor to fully recover the classical theory.

### 3.3 Inconsistencies in Previous Models

The critical examination of the classical theory in the preceding paragraphs reveals certain ambiguous aspects.

Firstly, discrepancies are evident in the authors' approach to determining the wave amplitude, denoted as  $\Omega_{vL}$  in Equation 2.88, when compared to the procedure employed for deducing the phase shift  $\Phi_{vc}$  in Equation 2.94. The quantity  $\Omega_{vL}$  is the wave amplitude that accounts for the mean axial motion of the liquid film, as shown by its derivation from the volumetric flow rate. Without any reasonable justification, the propagation velocity of disturbances,  $W_{w,vc}$  in Equation 2.87, is simply approximated to the wave velocity  $W_w$ . This approximation holds well only for calculating the wave amplitude  $\Omega_{vL,k}$  at the head-end of Closed-Head Open-End (CHOE) injectors and in the swirling chamber of Closed-Head Closed-End (CHCE) injectors, where the fluid is purely swirling. It is not appropriate when accounting for higher axial fluid motion in CHOE and OHOE injectors. In contrast, the phase shift  $\Phi_{vc}$  is correctly computed by considering the disturbance velocity as the sum of the wave velocity and the mean axial velocity of the liquid. The extended theory rectifies this inconsistency when setting  $B = 0$  and  $k_I = \omega/W_{w,vc}$ . The resultant impact on the injector transfer function is depicted in Figure 3.3. The curve shifts to lower val-

ues, and the amplitude of the response function diminishes more gradually with increasing frequency. The phase graphs remain largely unchanged.

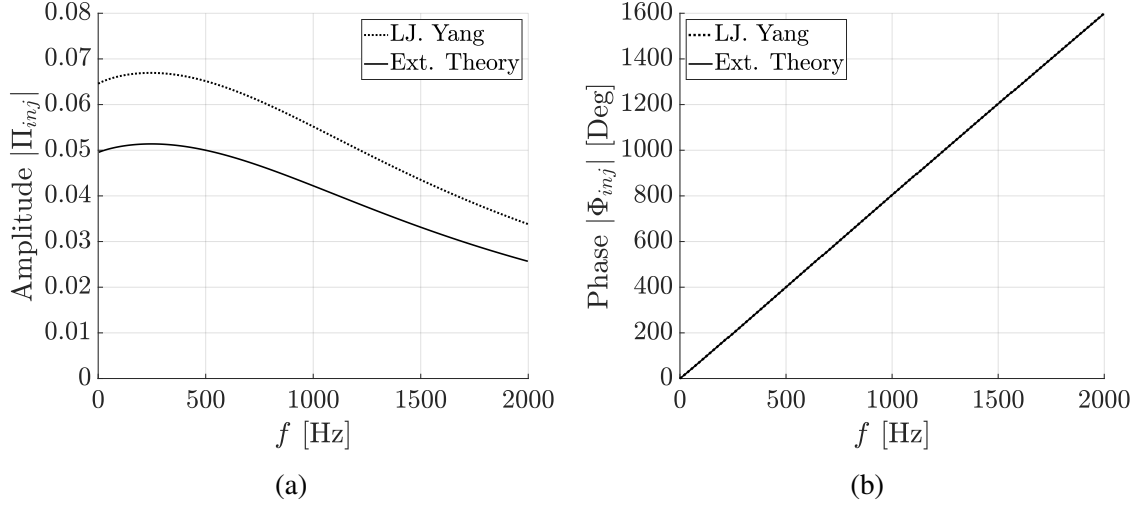


Figure 3.3: Impact on transfer function when accounting for mean axial liquid velocity in the wave propagation speed. The extended theory uses  $B = 0$  and  $k_I = \omega/W_{w,vc}$ .

Additional comparative analysis is illustrated in Figure 3.4. This analysis examines the repercussions of assuming  $W_{w,vc} = W_w$  in defining both the phase shift and wave amplitude. While consistent, this approach is not accurate due to the comparable magnitudes of fluid velocity and wave speed in the axial direction. The results indicate that the impact on the amplitude is smaller compared to the effect on the phase.

This analysis underscores the significant influence of the disturbance velocity used in defining  $\Omega_{vL}$  on the amplitude of the overall injector response, whereas a variation in the disturbance velocity defining the phase shift has a pronounced effect on  $\Phi_{vc}$ . Furthermore, due to the non negligible magnitude of the fluid axial motion, the latter should be always added to the wave speed for the total disturbance speed.

Secondly, a point of discussion is the response function associated with vorticity waves  $\Pi_{vcIII}$  expressed by Equation 2.98. Vorticity waves contribute to the instantaneous injector pressure drop and are contingent on centrifugal forces and tangential velocity pulsation. These waves are found at the injector head, where the tangential inlets are situated. Vor-

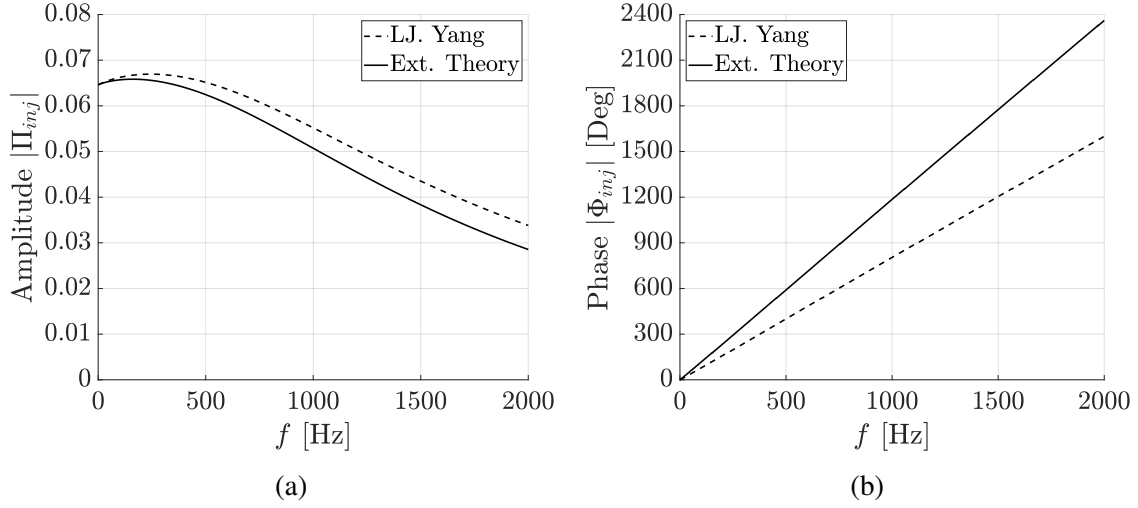


Figure 3.4: Impact on transfer function when not accounting for mean axial liquid velocity. The extended theory uses  $B = 0$  and  $k_I = \omega/W_w$ .

ticity waves propagate radially from the tangential inlet to the liquid free surface, decaying after very short distances in the axial direction [5, 22]. Due to the presence of liquid layers with different angular velocities, Professor Bazarov introduced viscous damping in  $\Pi_{vcIII}$  through the exponential term  $e^{-\nu f(\bar{x})}$ . This damping term has a significant impact on closed-end injectors, characterized by a thicker liquid film compared to open-end injectors. In fact, in the case of open-end injectors, Figure 3.5, removing the damping term practically does not affect the injector transfer function, with the maximum difference between the two curves being 0.3%. For this reason, the extended theory for OHOE injectors omits this term.

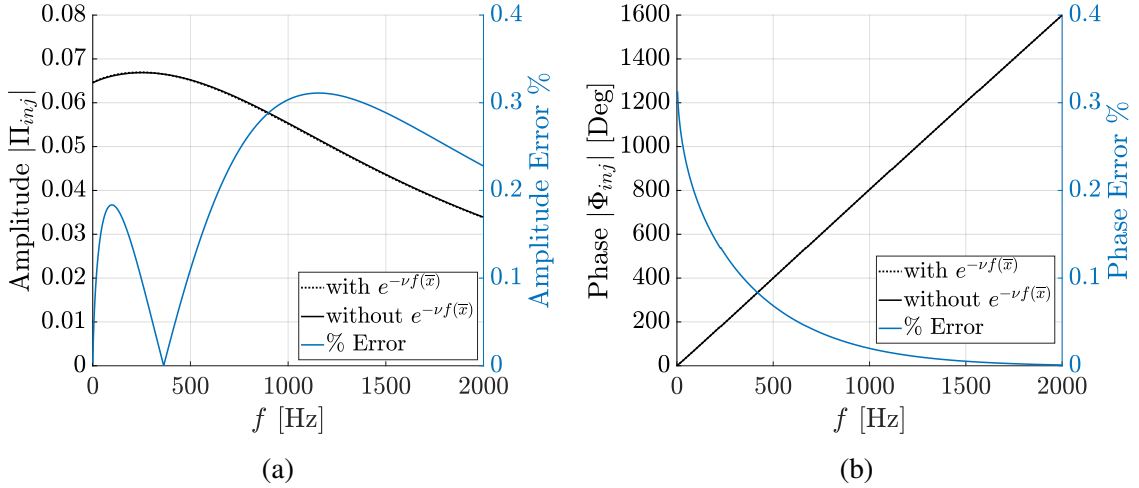


Figure 3.5: Impact on transfer function when removing the damping term in  $\Pi_{vcIII}$ .

### 3.4 Emulation of the Classical Theory

The development of the extended theory aimed to incorporate analytically the damping effects on propagating waves and introduce a new physical phenomenon—specifically, the shear stress exerted by the gas flow on the fluid. This inclusion renders the theory applicable to Open-Head Open-End (OHOE) injectors featuring coaxial gas flow. As addressed at the conclusion of Section 3.2, the extended theory mathematically converges to the classical model when setting the damping coefficient  $B$  to zero. Additionally, in Section 3.3, it was highlighted that, due to certain inconsistencies in prior models, the extended theory yields different results compared to the classical theory.

Nevertheless, a meaningful comparison can still be drawn between the general trends produced by the complete extended theory with  $B \neq 0$  and  $K_I = \omega/W_w$ , and the outcomes derived from the classical theory. To assess closed-head injectors, the transfer function can be computed through the extended theory while setting  $W_g$  to zero, indicating a stationary gas core. The geometries of interest are chosen from L.J. Yang's work [26] and are summarized in Table 3.1.

Table 3.1: Injector configurations employed for the comparative analysis between the extended and classical theory.

(a)		(b)	
Variable $L_{vc}/d_{vc}$		Variable $A$	
$L_{vc}$	75, 7 mm	$L_{vc}$	75 mm
$R_{vc}$	3.5 mm	$R_{vc}$	2.8, 4.2 mm
$r_{in}$	0.7 mm	$r_{in}$	0.7 mm
$L_T$	5 mm	$L_T$	5 mm
$A$	6.67	$A$	4, 10
$n$	3	$n$	3
$\Delta p_{inj}$	0.8 MPa	$\Delta p_{inj}$	0.8 MPa

### 3.4.1 Extended Theory

The results for a variable injector length to diameter ratio are shown in Figures 3.6 and 3.7. In the amplitude graphs, a conspicuous initial overshoot is observed at extremely low frequencies, followed by a comparable trend in both the classical and extended theories. Notably, the extended theory exhibits elevated values with increasing frequency. The disagreement is caused by several factors: the inconsistencies mentioned above, the employment of first approximation friction coefficients and the simplified linear approach.

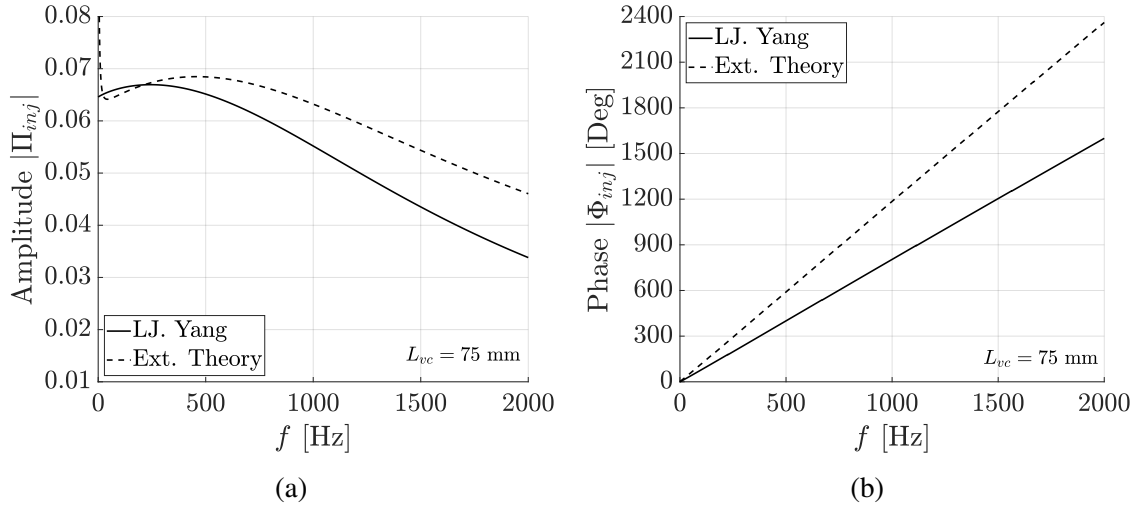


Figure 3.6: Extended vs Classical Theory – Amplitude and phase diagrams with  $L_{vc} = 75$  mm.

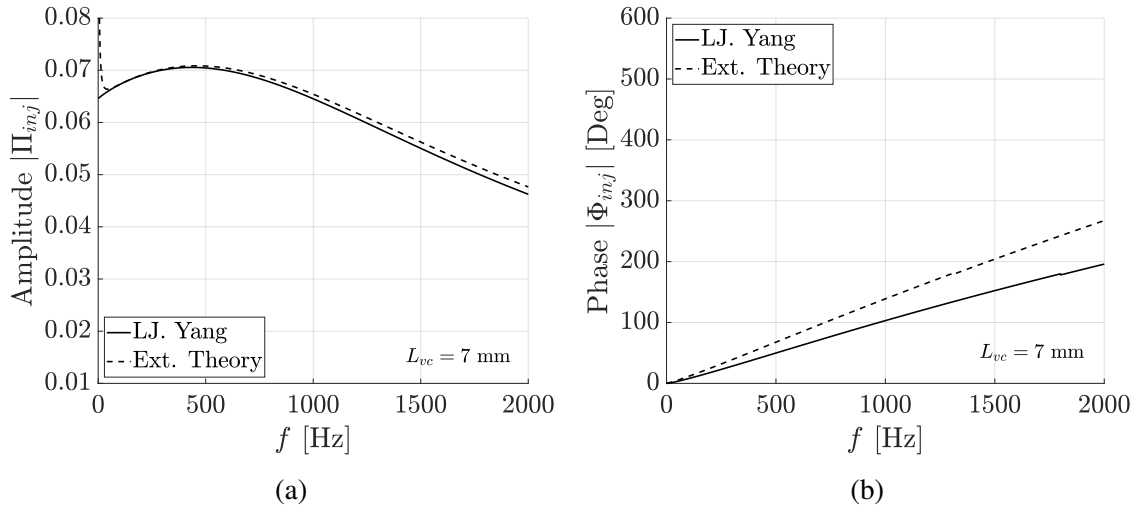


Figure 3.7: Extended vs Classical Theory – Amplitude and phase diagrams with  $L_{vc} = 7$  mm.

The coefficient  $C_f$  at the liquid-wall and gas-liquid interface necessitates a dependence on both the frequency of the liquid surface oscillation and the injector geometry. The latter is inherently contained within the Reynolds number ( $Re$ ), which is subjected to multiplication by an imprecise constant coefficient and exponentiation to an inaccurate power. It is noteworthy to observe that the overall agreement between the two curves for  $L_{vc} = 7$  mm is significantly enhanced as the damping effect in a shorter injector becomes less relevant.

The pronounced overshoot at low frequencies primarily derives from the high sensitivity of the extended theory in that range, a consequence of the linear approach adopted. The axial velocity pulsation depends on the frequency, differently from the classical theory. This strongly influences the volume flow rate pulsation and, consequently, the wave amplitude. The wave amplitude the the head-end of the injector tends to infinity (Equation (3.22)).

The impact of a distinct geometric characteristic  $A$  is depicted in Figure 3.8. The aforementioned trend remains applicable in this scenario, with the substantial amplitude contrast between low and high values of  $A$  being clearly delineated.

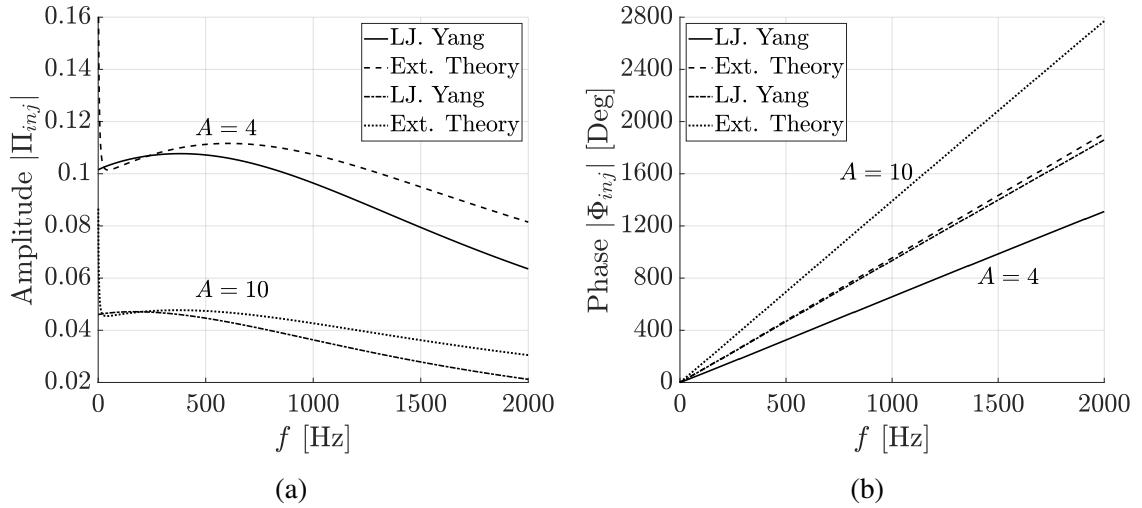


Figure 3.8: Extended vs Classical Theory – Amplitude and phase diagrams with  $A = 10$  and  $A = 4$ .

### 3.4.2 Asymptotic Theory

The correction of the overshoot at low frequencies is achieved through an asymptotic modification of the extended theory. The most relevant terms are denoted as  $Z_1$  and  $Z_2$ , defined as follows

$$Z_1 = \frac{\omega e^{k_i z}}{\sqrt{k_r^2 + k_i^2}} \quad (3.24)$$

$$Z_2 = e^{k_i z} \quad (3.25)$$

These terms appear in the  $D$  term of Equation (3.15) and the damping term in Equation (3.20). Their dependency on the frequency is illustrated in Figure 3.9.

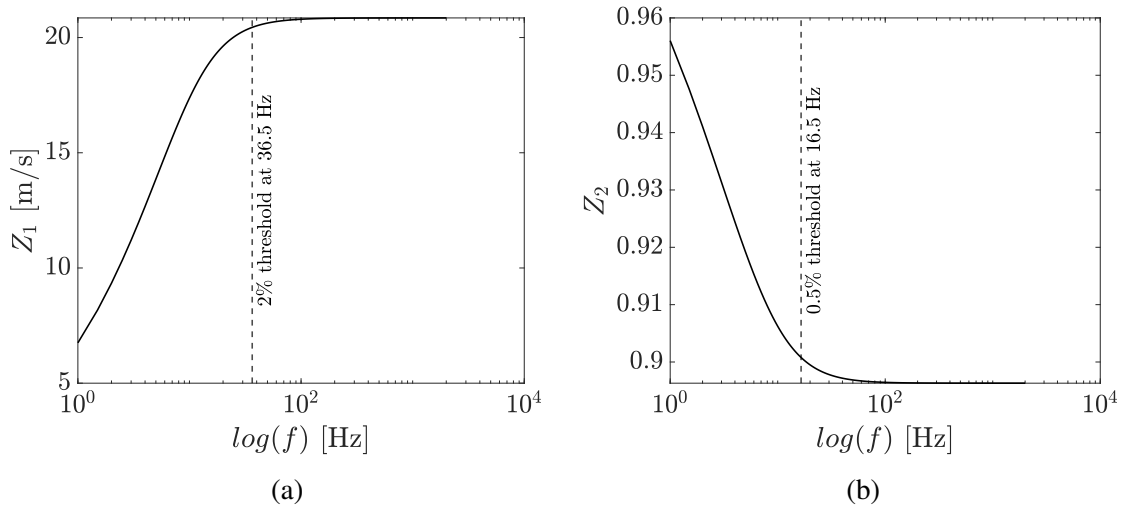


Figure 3.9: Evolution of  $Z_1$  and  $Z_2$  as a function of frequency. The threshold marks the frequency beyond which the  $Z_1$  and  $Z_2$  terms remain within 2% and 0.5%, respectively, of their values at 2000 Hz.

The logarithmic scale on the x-axis facilitates a clearer visualization of the evolution of  $Z_1$  and  $Z_2$  with increasing frequencies. The plots correspond to the case in Table 3.1a with  $L_{vc} = 75$  mm. Evidently, the quantities of interest immediately tend to a nearly constant value. The approximation of the  $Z$  terms with their value high frequency value remarkably improves the performance of the extended theory at low frequencies, as demonstrated in Figures 3.10 and 3.11.

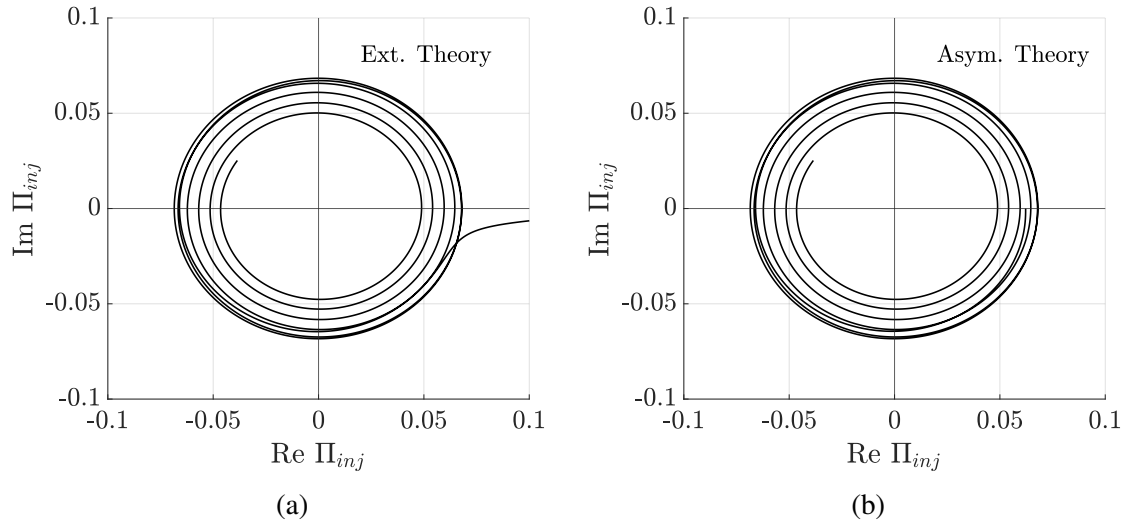


Figure 3.10: Extended vs Asymptotic Theory – Injector transfer function on the complex plane.

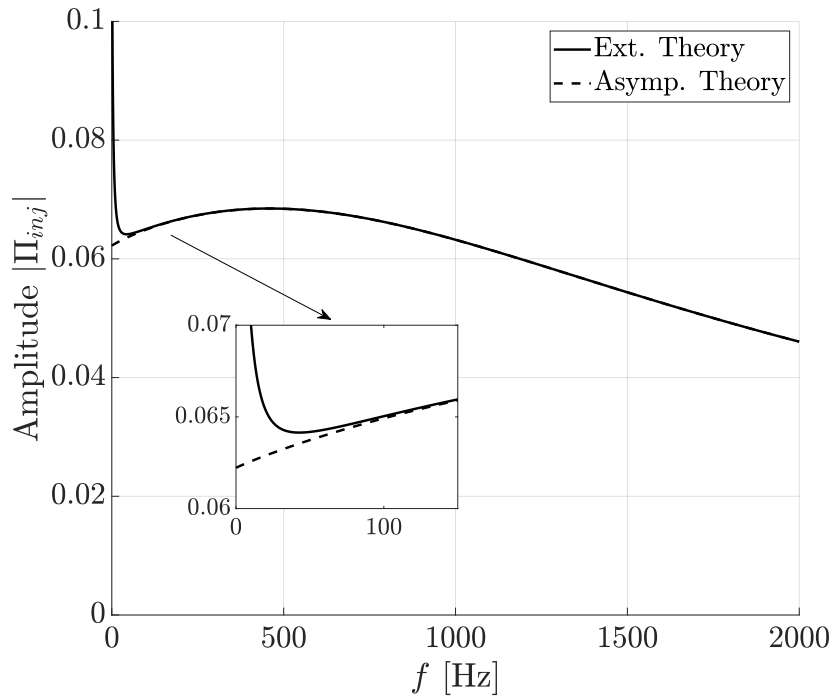


Figure 3.11: Impact of the asymptotic theory on the injector transfer function at low frequencies.

However, the asymptotic approach fails to capture certain effects on the anticipated transfer function. Specifically, the amplitude peak of the response function occurs at a

fixed frequency for varying injector lengths, as prominently depicted in Figure 3.12. This theoretical limitation is further addressed and improved upon in Section 3.4.3.

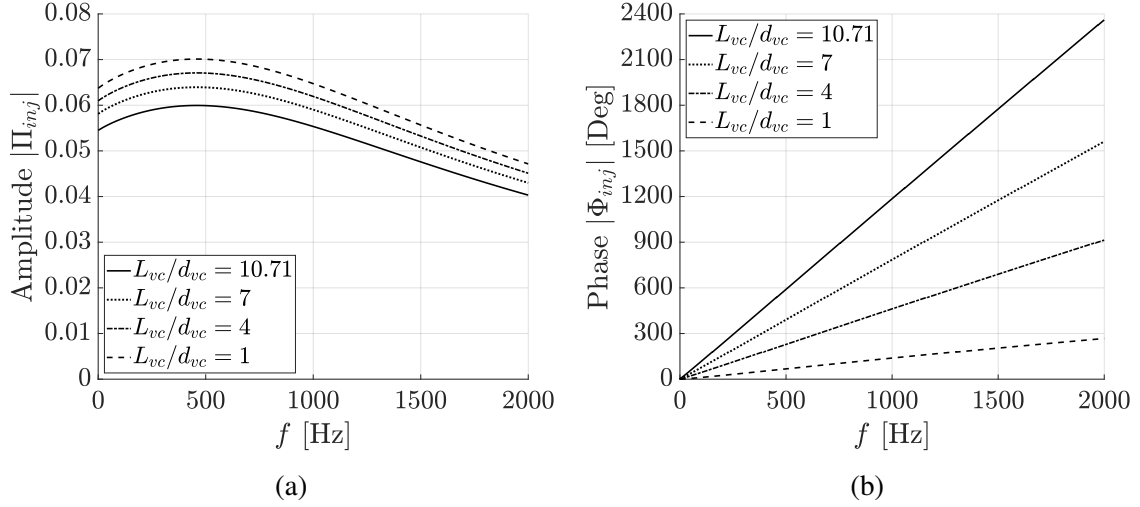


Figure 3.12: Asymptotic Theory – Impact of injector length on the injector transfer function.

### 3.4.3 Optimized Extended Theory

The exponential damping  $Z_2$  (Equation (3.25)) analytically derived in the extended theory is comparable to the exponential  $e^{-\nu\Phi_{vc}/2\pi}$  derived by Bazarov in the classical model. The latter term decreases significantly with increasing frequencies, indicating a more intense damping on high-frequency waves. Consequently, the approximation of  $Z_2$  with its asymptotic value is inappropriate. Furthermore,  $Z_2$  stabilizes to a value near unity. This analysis implies that modifying  $Z_2$  is necessary to achieve the anticipated behavior across the frequency range of interest. Effective results are obtained through the adjustment of the friction factors governing shear stress. An examination of the  $B$  term in the forced wave equation, responsible for damping waves, reveals that the contribution of the wall is considerably greater than the shear stress at the gas-liquid interface. Notably, with a reasonable value set for both friction factors being  $10^{-4}$ , due to the substantial density difference

between gas and liquid

$$C_{f,lw} \overline{W}_{av} \gg \frac{\rho_g}{\rho_l} C_{f,lg} (\overline{W}_{av} - W_g) \quad (3.26)$$

This significant difference holds true for a stationary gas core, but it remains valid for a typical axial gas velocity in gas turbine engines (100 – 200 m/s). The evaluation of the axial liquid-to-air MFR provides an additional reason to consider the gas shear stress on the liquid surface as small. For an axial liquid velocity of 10 – 30 m/s and gas velocity of 200 m/s, the momentum flux ratio is 2.5 – 22.5. Consequently, it is reasonable to firstly apply changes to the liquid-wall friction factor, neglecting the gas-liquid friction coefficient.

The goal is to introduce frequency dependence in  $C_{f,lw}$ . A potential approach is a first-order polynomial that is a function of the disturbance pulsation frequency, as follows

$$C_{f,lw}^* = C_{f,lw} (x_1 + x_2 \omega) \quad (3.27)$$

where  $x_1$  and  $x_2$  are tuning coefficients. Using the classical theory as a reference for a stationary gas core ( $W_g = 0$ ), the coefficients can be determined through an optimization algorithm aiming to minimize the difference between the analytical and experimental damping factor, defined as

$$err = \sum_{i=1}^n |e^{k_i L_{vc}} - e^{-\nu \Phi_{vc}/2\pi}| \quad (3.28)$$

for the discretized angular frequency  $\omega_i = 0, \dots, 4000\pi$  rad/s. The correction applied to  $C_{f,lw}$  introduces a linear dependency on the frequency and it prevents the friction factor from becoming null as  $\omega$  tends to zero. Particle swarm optimization is employed to search for the most appropriate coefficients in several cases, yielding interesting results. The graphs of the injector transfer function for the geometrical configurations studied by L. Yang are depicted in Figure 3.13. The optimal coefficients are  $x_1 = 2.447 \times 10^{-4}$  and

$x_2 = 2.510 \times 10^{-4}$  s/rad and the optimization is robust with respect to the injector length. The results closely resemble those presented at the conclusion of Section 2.2.3 and any discrepancies are attributed to the inconsistencies explained in Section 3.3.

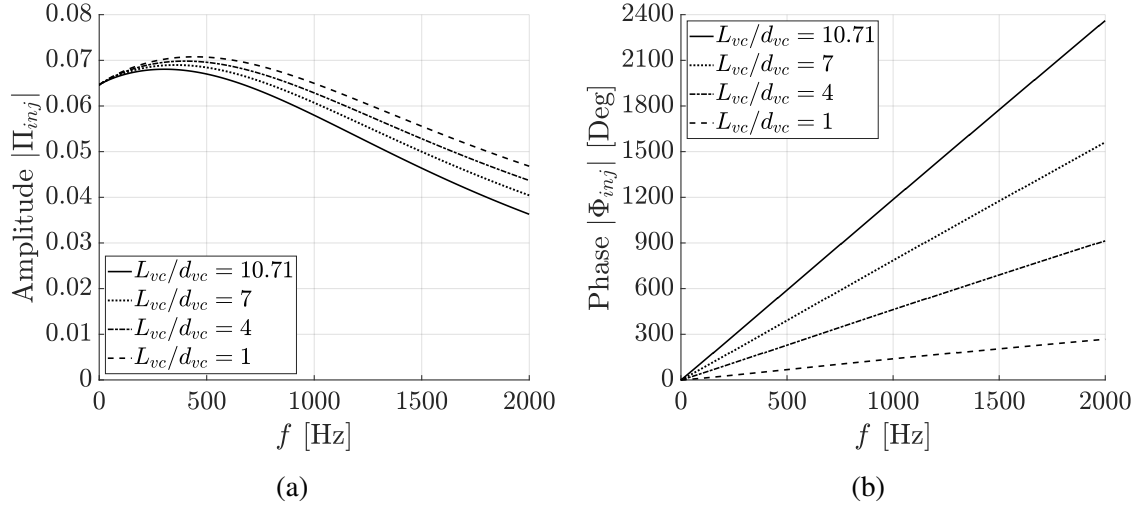


Figure 3.13: Optimized Theory – Impact of injector length on the injector transfer function.

The results presented in this section highlight the potential of adjusting the friction factors to improve the extended theory. While this was demonstrated using experimental results as a reference, it is crucial to emphasize that high-fidelity CFD simulations can play a fundamental role in calibrating the friction factors in future work.

### 3.5 Parametric Study

The examination of the impact of geometrical parameters on the injector transfer function is essential for predicting injector performance and facilitating the design process. The primary parameters of interest include injector length, geometric parameter  $A$ , pressure drop across the injector and axial gas velocity. All investigations are conducted utilizing the optimized extended theory with  $K_I = \omega/W_{w,vc}$ , ensuring freedom from inconsistencies. Moreover, the calibration of the liquid-wall friction coefficient for varying injector parameters provides insights into the trends of tuning coefficients.

### 3.5.1 Injector Length

The parameters characterizing the injector configurations employed in this study are detailed in Table 3.1a, with the exception of  $L_{vc}$ . The choice of injector length is specified as a multiple of the injector diameter, as outlined in Table 3.2, which also includes the coefficients  $x_1$  and  $x_2$ . The optimization coefficients remain consistent for every injector length, showing robustness with respect to this parameter. The effect of length variation on the injector transfer function is illustrated in Figure 3.14. Increasing the injector length results in a reduction of mass flow rate oscillation amplitude for a given pressure oscillation, attributed to the increased damping due to the longer distance traveled by the waves. Similarly, the phase shift becomes larger with increased length.

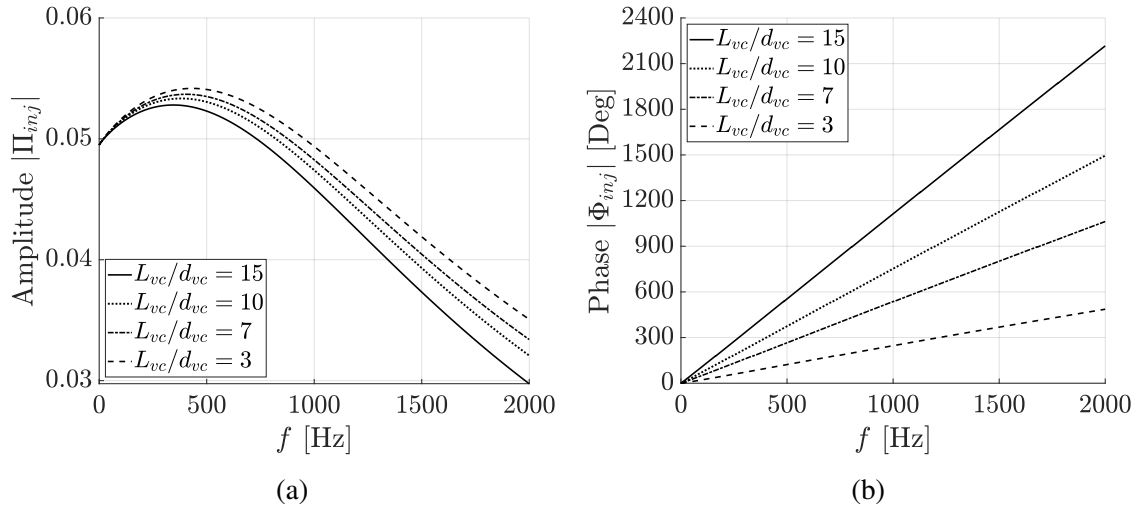


Figure 3.14: Optimized Theory Parametric Study – Impact of injector length on the injector transfer function.

Table 3.2: Tuning coefficients for different injector lengths.

Variable $L_{vc}$				
$L_{vc}$ [mm]	105	70	49	7
$x_1$	$2.447 \times 10^{-4}$			
$x_2$ [s/rad]	$3.751 \times 10^{-4}$			

### 3.5.2 Geometric Characteristic Parameter

The study for different values of the geometric characteristic parameter is conducted using the parameters in Table 3.1b. The complete set of injector radius values and the corresponding  $A$  values are in Table 3.3, which also includes the optimization coefficients. Notably, these coefficients exhibit an ascending trend with increasing  $A$ , and a second-order polynomial is employed to interpolate the data for  $A = 4 - 10$ . Consequently, the values of  $x_1$  and  $x_2$  for  $A = 14$ , denoted in bold, are predicted using the interpolating polynomial and compared to the values obtained through the optimization process applied to the other  $A$  values. The predicted and the calculated values show close agreement. The observed variation in the coefficients with increasing  $R_{vc}$  suggests that the  $Re$  number in the first-approximation friction factor is raised to an inaccurate exponent. The trend for the optimization coefficients and the injector transfer function are depicted in Figures 3.15 and 3.16, respectively. The physical interpretation of the geometric parameter elucidates the observed results:  $A$  represents the swirling strength of the liquid, leading to wave attenuation as  $A$  increases. Moreover, as  $A$  increases,  $W_{w,vc}$  decreases, causing an increase in the phase shift since  $\Phi_{vc} = k_i L_{vc} = f(1/W_{w,vc})$ .

Table 3.3: Tuning coefficients for different values of the geometric characteristic parameter. The values in bold are predicted by the interpolating polynomial based on the other values.

Variable $A$					
$A$	4	6.67	8	10	14
$R_{vc}$ [mm]	2.8	3.5	3.8	4.2	4.9
$x_1 (\times 10^{-4})$	2.418	2.447	2.459	2.474	<b>2.498</b>
$x_2 (\times 10^{-4})$ [s/rad]	3.288	3.751	3.928	4.141	<b>4.458</b>

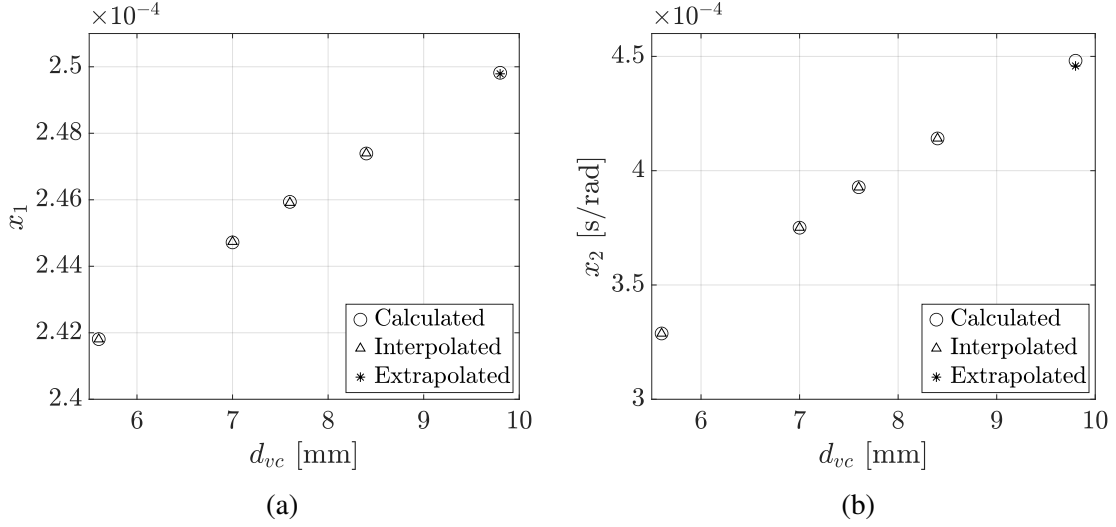


Figure 3.15: Tuning coefficients as a function of  $d_{vc}$ .

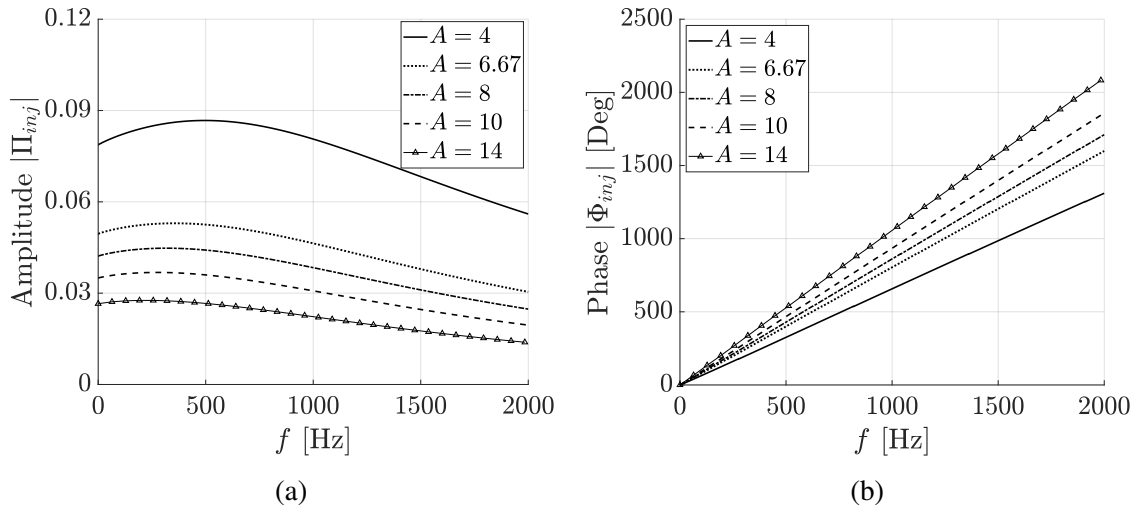


Figure 3.16: Optimized Theory Parametric Study – Impact of geometric characteristic parameter on the injector transfer function.

### 3.5.3 Pressure Drop

Pressure drop effects are studied for a given geometry (Table 3.1a with  $L_{vc} = 75$  mm) and various values of  $\Delta p_{inj}$  as listed in Table 3.4. The table includes the tuning coefficients for each case, and values in bold are predicted through a second-order polynomial that interpolates the  $x$  coefficients for  $\Delta p_{inj} = 0.4 - 1.2$  MPa. The predicted values lack accuracy due to the limited amount of interpolated data, but the expected trend of the response function

for  $\Delta p_{inj} = 0.25$  and  $1.6$  MPa is achieved. The variation in the optimization coefficients is linked to the inaccurate dependency of the friction factor on the  $Re$  number. In fact, varying the pressure drop across the injector implies a change in liquid velocity. This result is comparable to the results obtained for a varying geometric characteristic parameter. The amplitude and phase of the injector response function are illustrated in Figure 3.18.

Table 3.4: Tuning coefficients for different values of the injector pressure drop. The values in bold are predicted by the interpolating polynomial based on the other values.

Variable $\Delta p_{inj}$					
$\Delta p_{inj}$ [MPa]	0.25	0.4	0.8	1.2	1.6
$x_1 (\times 10^{-4})$	<b>2.148</b>	2.244	2.447	2.574	<b>2.625</b>
$x_2 (\times 10^{-4})$ [s/rad]	<b>5.432</b>	4.864	3.751	3.222	<b>3.276</b>

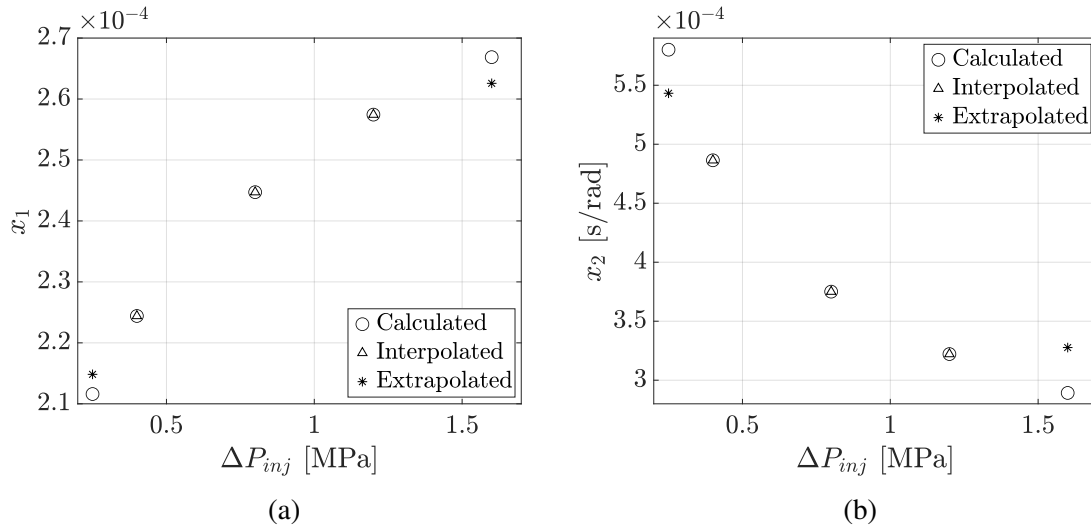


Figure 3.17: Tuning coefficients as a function of  $\Delta p_{inj}$ .

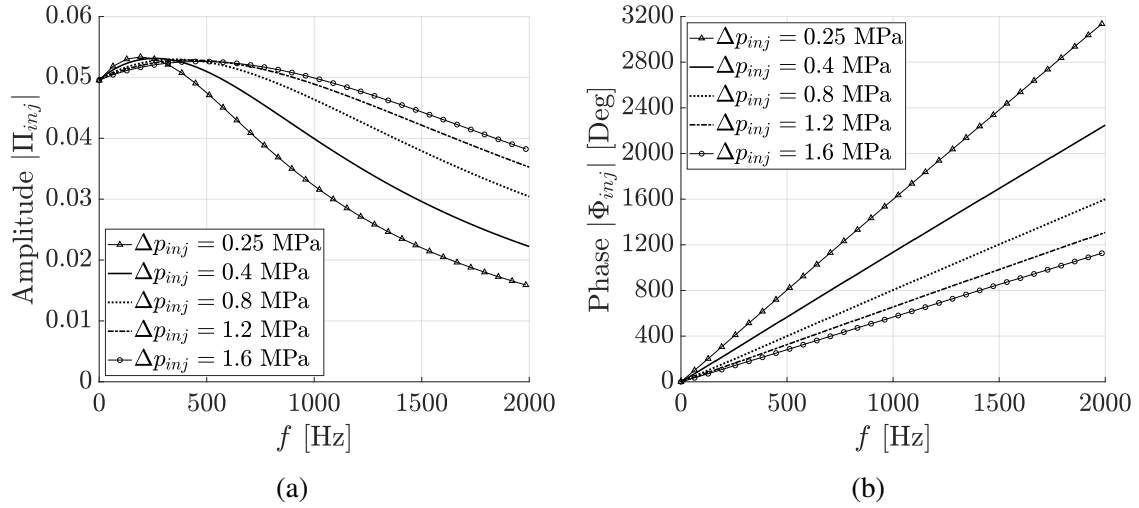


Figure 3.18: Optimized Theory Parametric Study – Impact of injector pressure drop on the injector transfer function.

### 3.5.4 Gas Velocity

The influence of axial gas velocity on the overall injector transfer function is examined for a fixed geometry (Table 3.1a with  $L_{vc} = 75$  mm) and typical gas velocities encountered in practical applications. As observed in Figure 3.19, the effect of the gas shear stress on the liquid surface results to be small. This can be attributed to the significantly higher momentum flux ratio of the liquid phase compared to the gas phase. While numerical simulations could provide deeper insights into the accuracy of this result and offer guidance on the tuning of the gas-liquid friction coefficient, if required, it is noteworthy that the extended theory adequately captures the effects associated with gas shear stress, yielding a minor contribution. Moreover, future investigations could explore the introduction of additional physical effects. For instance, a pressure distribution on the liquid surface that depends on the liquid surface instantaneous slope could be an interesting approach to explore.

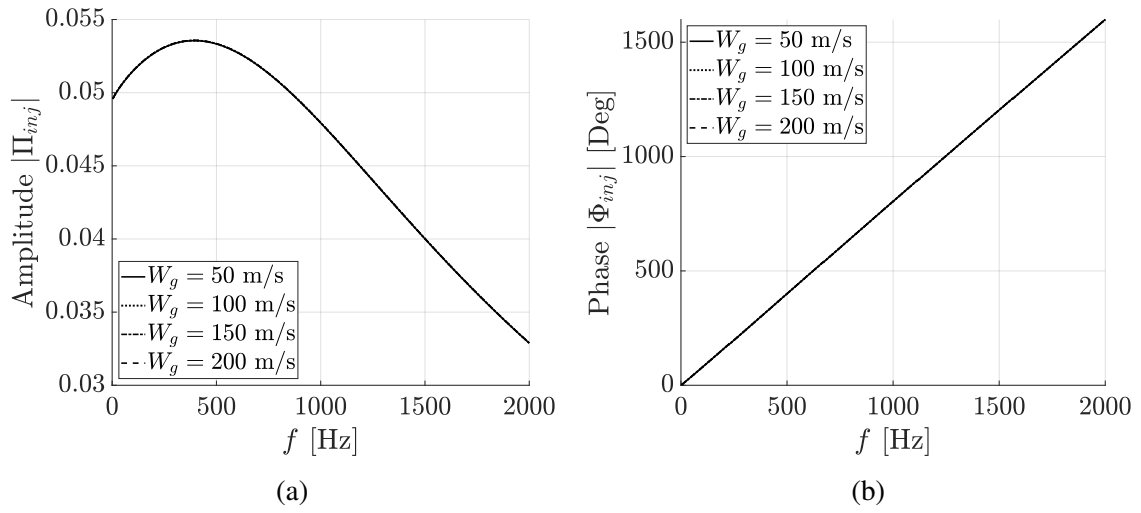


Figure 3.19: Optimized Theory Parametric Study – Impact of gas velocity on the injector transfer function.

## CHAPTER 4

### NUMERICAL INVESTIGATION

The Computational Fluid Dynamics solver used for this work is Ansys<sup>®</sup> Fluent. The objective of the numerical study is to provide a qualitative description of the flow physics in an OHOE coaxial swirl injector. The study is conducted for a 2D axisymmetric domain. Due to the difficulties in generating an appropriate initialization for steady Reynolds-Averaged Navier–Stokes (RANS), the unsteady counterpart is used. The validation reference for the CFD approach is Chen’s work [49]. Several turbulence models are employed to evaluate their ability to replicate the previous work aiming to reduce the total computational cost. Multiple mesh resolutions are used and the differences assessed.

#### 4.1 Preliminary Study

A preliminary study is conducted with the objective of selecting a turbulence model, domain and mesh able to qualitatively simulate the flow physics involved in OHOE swirl injectors. This specific injector configuration has never been studied before, therefore the model cannot be validated replicating a previous work with the exact same physics. However, for the understanding of the main flow characteristics, the validation and model selection is performed against the work by Chen [49] for a CHCE swirl injector.

Chen simulated the swirling flow using Reynolds Stress Model (RSM) for a 2D axisymmetric geometry and the results are successfully replicated as shown in Figure 4.1. Due to the anisotropic nature of the stress tensor, RSM requires the solution of seven equations and it renders the model computationally expensive. Consequently, several other turbulence models are tested aiming to find a valid alternative to RSM for faster calculations. The results obtained through  $k - \epsilon$  Re-Normalization Group (RNG),  $k - \epsilon$  RNG with swirl correction, realizable  $k - \epsilon$  and  $k - \omega$  Shear Stress Transport (SST) are depicted in

Figures 4.3 and 4.4. The comparison is facilitated overlaying the liquid-gas interface for each model in Figure 4.2. The realizable  $k - \epsilon$  model produces non-physical results. Re-Normalization Group  $k - \epsilon$  exhibits a non-physical representation in the swirling chamber, where the swirl is the dominant characteristic of the flow. Enabling the swirl correction partially improves the results in the swirling chamber, but the swirling radius at the free surface increases in the axial direction. Moreover, strong oscillations are produced in the nozzle. The best qualitative result is obtained through  $k - \omega$  SST that produces a flat liquid surface in the swirling chamber despite the swirling radius is slightly underestimated. In addition, the oscillations in the nozzle are greatly attenuated but the spray angle is well represented. The analysis of the turbulence models suggests the  $k - \omega$  SST as the most suitable for a qualitative investigation and a significantly lower computational cost.

The simulation of a CHOE injector is also performed. The objective is to validate the CFD approach with respect to the inviscid steady-state theory for an open-end configuration. The volume fraction contour plot is depicted in Figure 4.5. The injector parameters are summarized in Table 4.1. As a reference, the liquid surface swirling radius at the head-end and near the injector exit are compared to the theoretical predictions in Table 4.2.

Table 4.1: OHOE injector configuration.

$R_{vc}$ [mm]	$r_{in}$ [mm]	$L_{inj}$ [mm]	$L_T$ [mm]	$\dot{m}_{in}$ [kg/s]	$n$
5	0.65	30	4	0.09	3

Table 4.2: Theoretical and numerical swirling radius of the liquid surface.

	$r_{mk}$ [mm]	$r_{mn}$ [mm]
CFD	4.2175	4.6647
Theory	4.3482	4.5618
% Error	3.00	2.26

Figure 4.1: Validation against Chen's results with RSM.

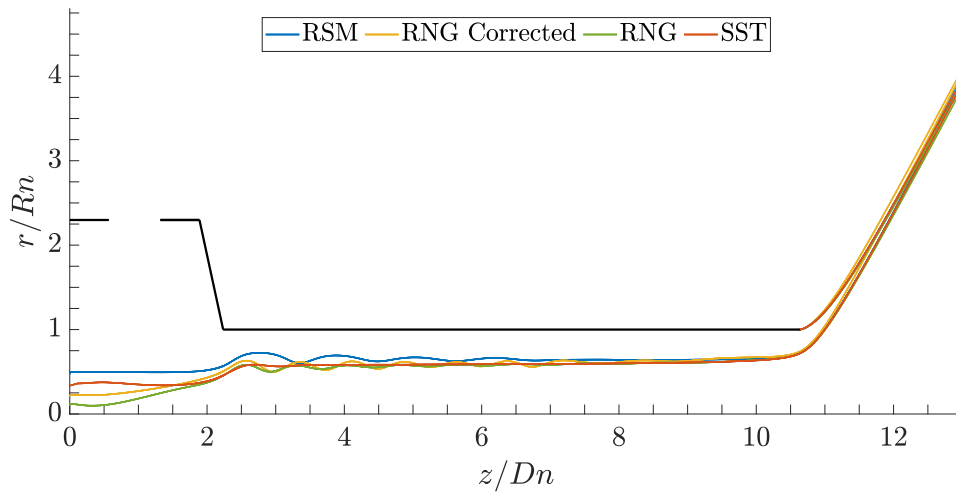
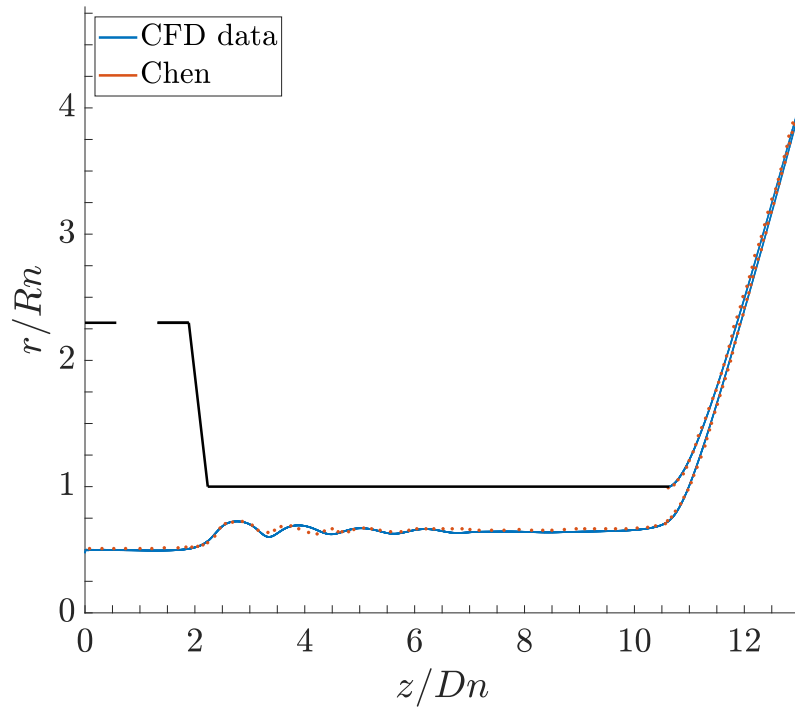


Figure 4.2: Turbulence models on Chen's injector.

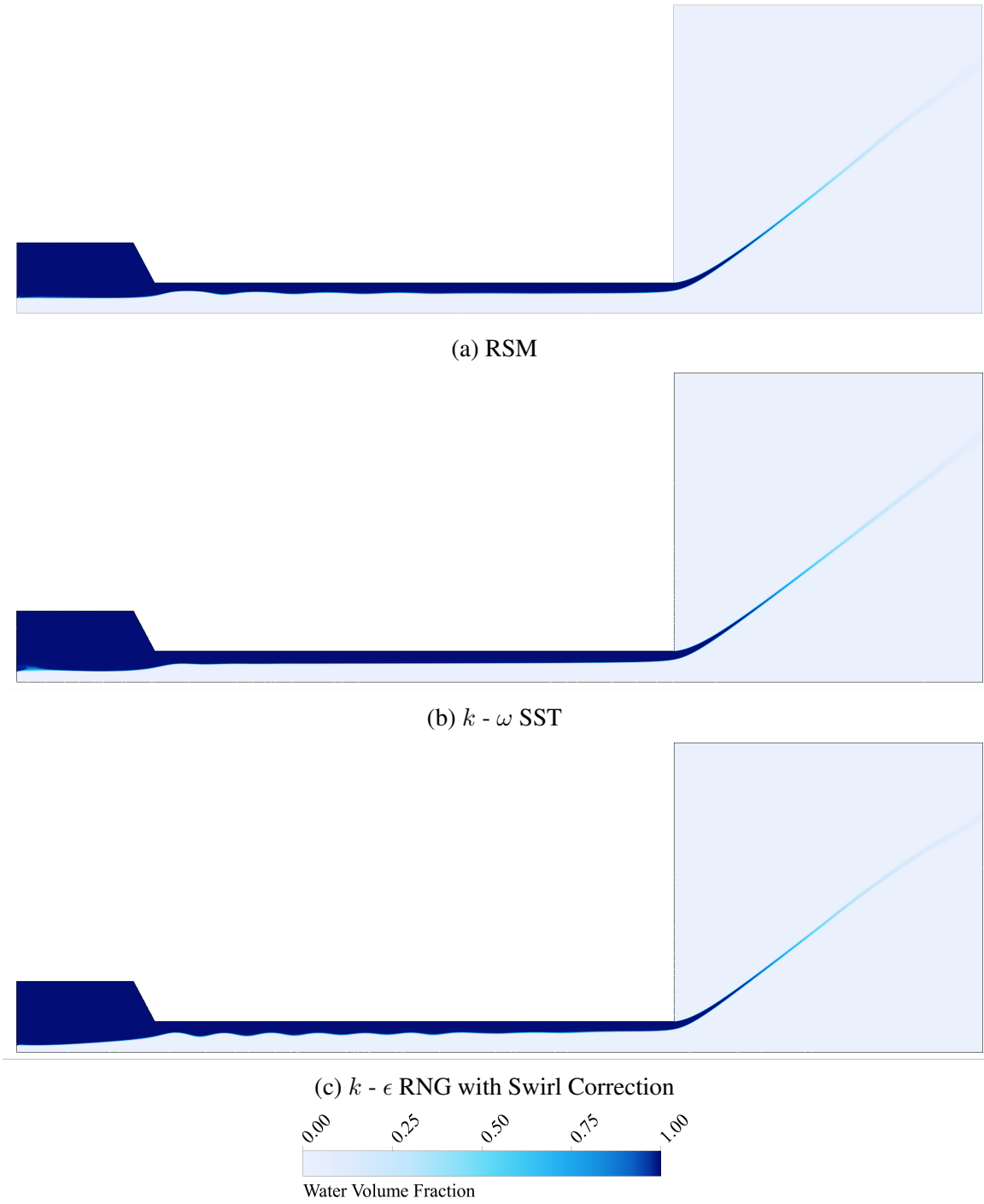


Figure 4.3: Volume fraction in Chen's injector for different turbulence models.



(a)  $k - \epsilon$  RNG



(b)  $k - \epsilon$  Realizable

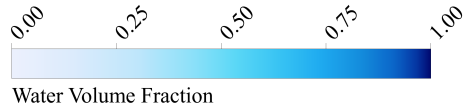


Figure 4.4: Volume fraction in Chen's injector for different turbulence models.



Figure 4.5: Inviscid CHOE injector.

## 4.2 Geometry and Mesh

The geometry used for the viscous simulations of the OHOE injector is similar to the configuration used in the inviscid case (Table 4.1). An extension of 6 mm at the head end renders the domain appropriate to introduce a gas inlet and analyze the swirling liquid moving upstream. The domain includes the injector and a downstream region extending for  $14 D_{vc}$  and  $6 D_{vc}$  in the axial and radial direction, respectively. Therefore, the downstream region is stretched in the axial direction, that is the predominant flow direction at the injector exit. This is a consequence of the high speed gas flow. The domain is depicted in Figure 4.6.

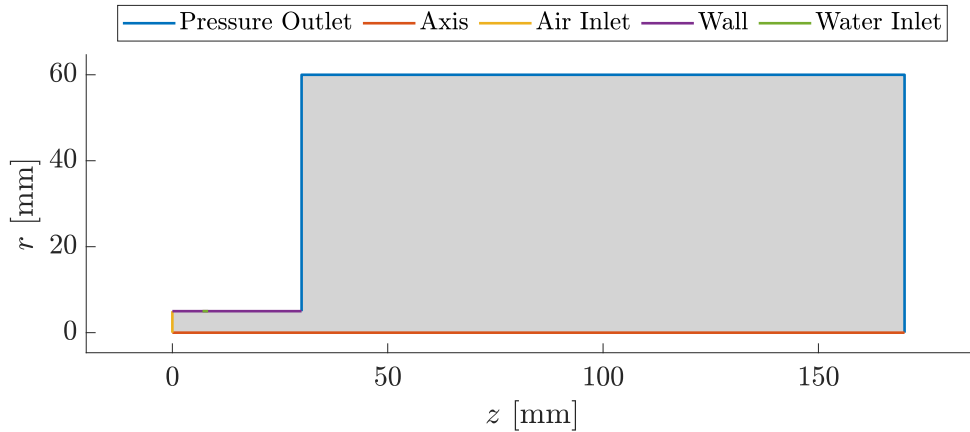


Figure 4.6: Injector domain and downstream region.

Three different structured meshes discretize the domain. The coarsest mesh is characterized by a  $100 \times 1020$  grid inside the injector, depicted in Figure 4.7. Dividing each element side by square root of two produces a more refined mesh with a grid of  $142 \times 1444$  doubling the cells of the coarse mesh. Finally, the finest mesh is defined by a  $300 \times 1530$  grid. The latter mesh is distinguished by slowly growing inflation layers starting from the injector wall. At the injector exit and downstream region, the cells gradually vary in size ensuring a high quality mesh, as illustrated in Figure 4.8. Moreover, an adaptive mesh refinement at the liquid-gas interface increases the resolution of the free liquid surface.



Figure 4.7: Coarse mesh.

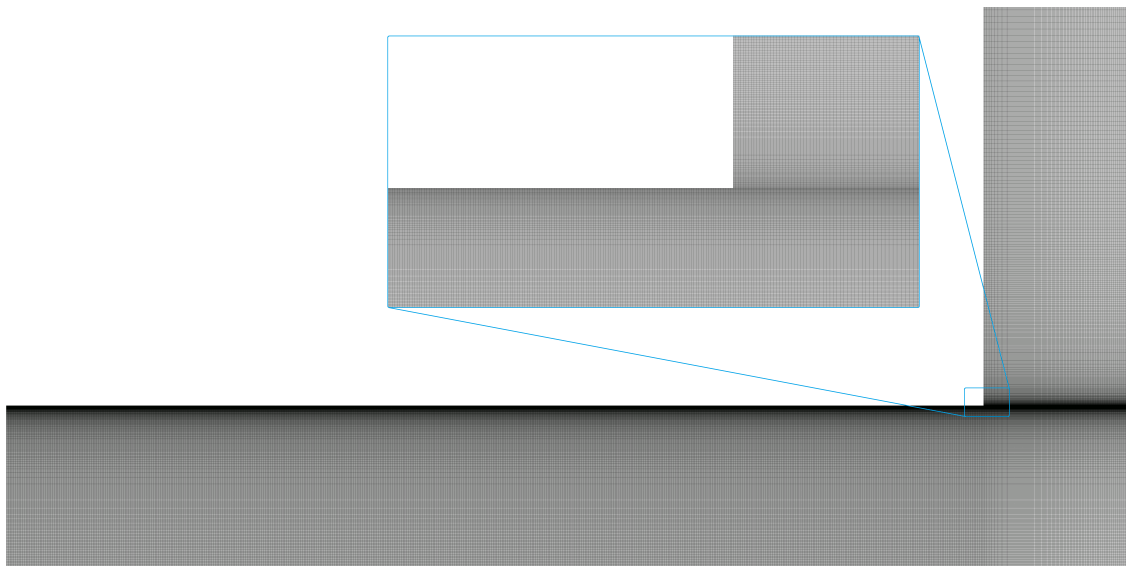


Figure 4.8: Fine mesh with inflation layers.

## 4.3 Solver Setup

### 4.3.1 Numerical Models

The simulations are performed with a pressure-based solver on a 2D axisymmetric domain. The OHOE coaxial swirl injector involves a two-phase flow field, specifically liquid and gaseous. Incompressible air at standard conditions models the gas phase ( $\rho_g = 1.225 \text{ kg/m}^3$ ), while water at constant density  $\rho_l = 998.2 \text{ kg/m}^3$  represents the liquid phase. The multiphase problem is solved by means of a volume of fluid method with an implicit formulation and a dispersed interface modeling. The surface tension coefficient is maintained constant at  $0.07275 \text{ N/m}$ . The difficulties encountered to correctly initialize a steady-state solution lead to the use of URANS. In all cases, the injector is initialized filled with air at ambient pressure. Reynolds Stress Model is employed with non-equilibrium wall functions. The  $k - \omega$  SST model is used with the addition of a damping mechanism of the turbulent viscosity within the interfacial region. The pressure-velocity coupling term is treated through the SIMPLE scheme and the spatial discretization for pressure is achieved by means of the PRESTO! method. The momentum and all the other equations involved are discretized with a second-order upwind scheme.

An adaptive mesh refinement improves surface capturing and stability of the simulations. The mesh is refined at the liquid-gas interface every 4 time-steps and the maximum level of refinement is set to be 3. The minimum cell size is  $2 \mu\text{m}$ . The refined mesh is clearly visible in Figure 4.9.

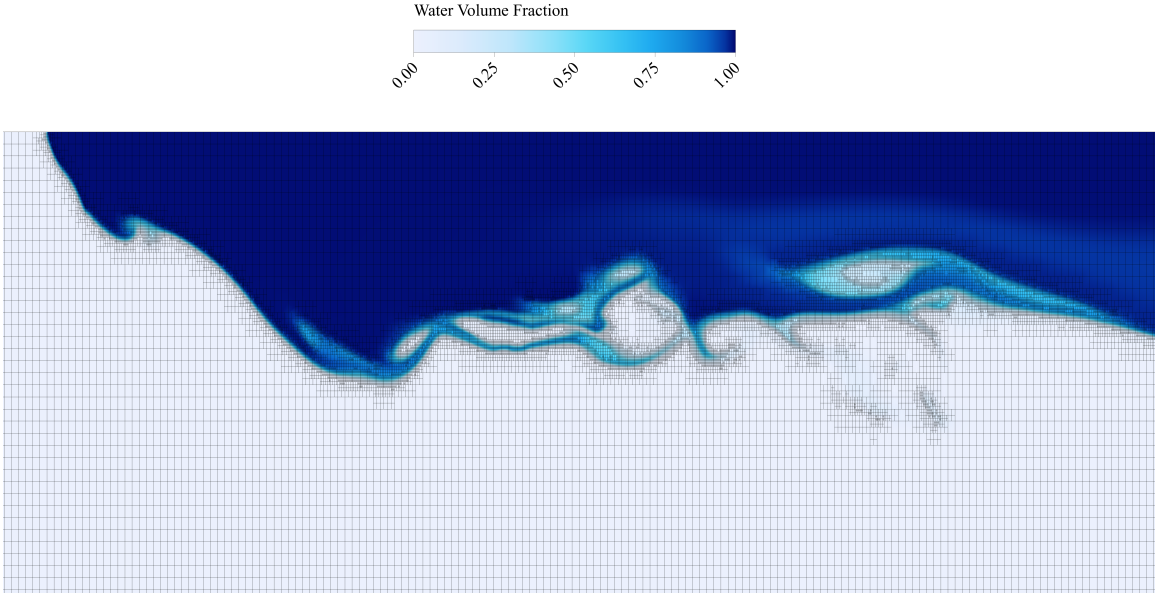


Figure 4.9: Zoom on mesh refinement at the liquid-gas interface in an instantaneous snapshot of RSM.

#### 4.3.2 Boundary Conditions

The boundary conditions applied on the domain are summarized in Figure 4.6. The air inlet was selected as a velocity inlet specifying the velocity magnitude in the direction normal to the boundary. The water inlet is a velocity inlet where the radial and tangential component are calculated for mass flow rate and angular momentum conservation. The 2D axisymmetric nature of the domain implies that a discrete injection through tangential inlet channels cannot be modelled. Rather, liquid injection occurs continuously across a slit of thickness  $2r_{in}$ . The angular momentum of the liquid entering the injector through tangential channels is obtained as

$$C = W_{in}R_{in} \quad (4.1)$$

where  $W_{in}$  can be found from the inlet mass flow rate  $\dot{m}_{in}$  and  $R_{in} = R_{vc} - r_{in}$ . Therefore, the inlet tangential velocity in the 2D domain is derived as follows

$$W_T = \frac{C}{R_{vc}} \quad (4.2)$$

The inlet radial velocity, instead, ensures the conservation of the  $\dot{m}_{in}$  through the slit

$$W_r = \frac{\dot{m}_{in}}{\rho_l F_{slit}} \quad (4.3)$$

The other boundaries that define the injector are a no-slip wall and the axis to define the symmetry. The downstream region is bounded by three pressure outlets where the pressure is set to 0.1 MPa.

#### 4.4 Numerical Results

The tangentially injected liquid gains axial velocity moving away from the slit inlet while maintaining a strong swirling motion. The momentum carried by the liquid is greater than the gas axial momentum, therefore the liquid tends to move upstream besides the axial downstream motion. The gas immediately interacts with the liquid and a thick liquid region forms between the two inlets. The parameters chosen for the OHOE configuration produce a remarkably thin liquid layer. This enhances the formation of surface waves on the liquid that propagate towards the injector exit and induce an unstable spray. The oscillations on the liquid surface and the spray characteristics are sensitive to the model used for the calculations. The differences between RSM and  $k - \omega$  SST on the coarse mesh are depicted in Figure 4.10. The former method produces a greatly diffused interface with respect to  $k - \omega$  for the same local mesh refinement. The same behavior is observed on the refined meshes in Figure 4.11, where RSM is employed for the medium mesh and  $k - \omega$  for the finest mesh with inflation layers. Although the comparison on different mesh resolutions is not rigorous, this confirms what the coarse mesh shows. Doubling the number of cells for RSM calculations does not significantly impact interface capturing, while  $k - \omega$  SST reveals intricate wave details. Moreover, the liquid spray produced by  $k - \omega$  is thinner and breaks up sooner. The introduction of inflation layers considerably lowers  $y^+$  value along the injector wall. In fact, nearly all the cells have  $y^+ < 2$  as shown in Figure 4.12 and

this improves the treatment of the turbulent boundary layer as it ensures the first cell lies within the viscous sublayer. A higher gas velocity results in the formation of a shorter liquid region and more pronounced surface oscillations, as depicted in Figure 4.13.

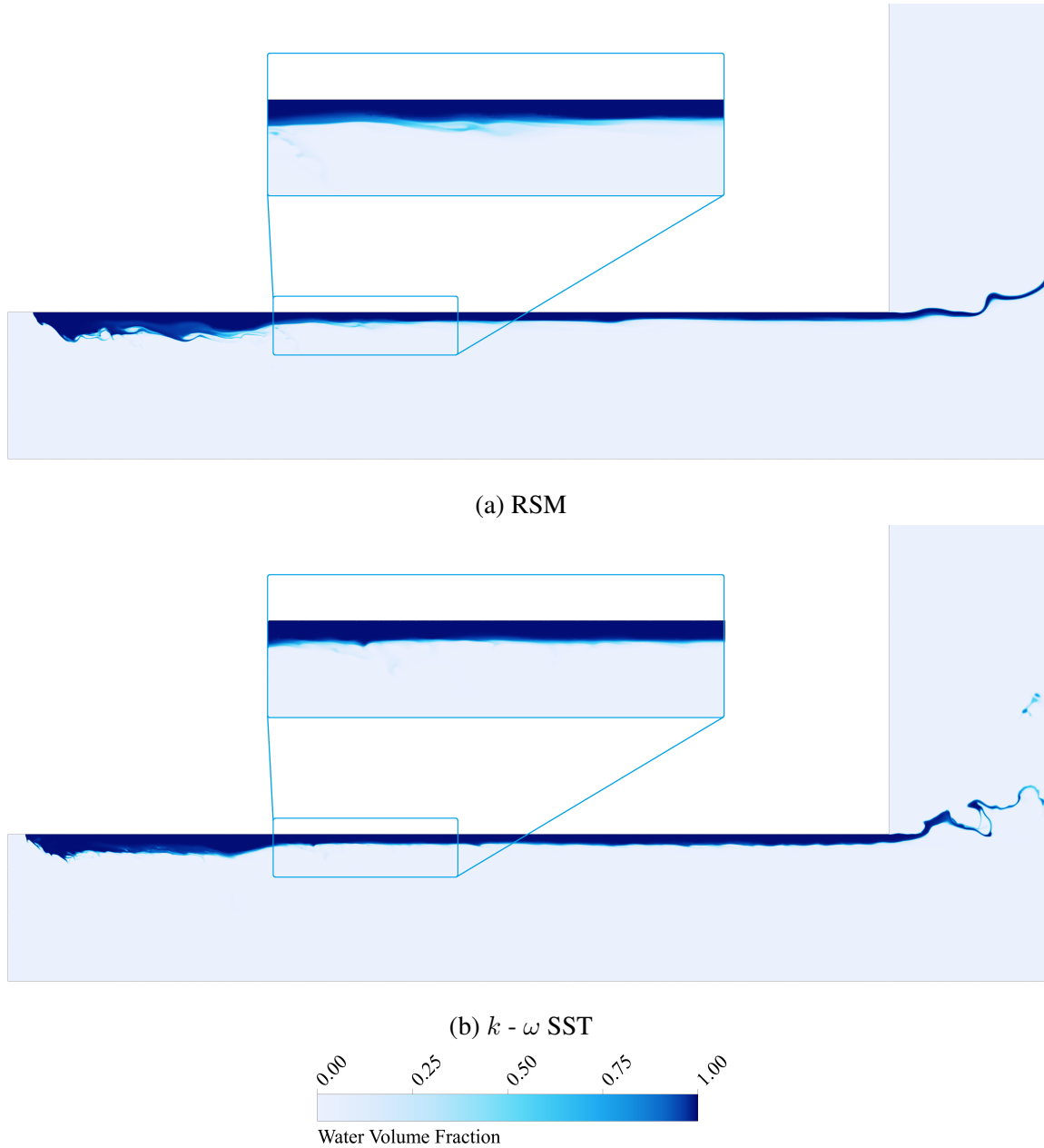
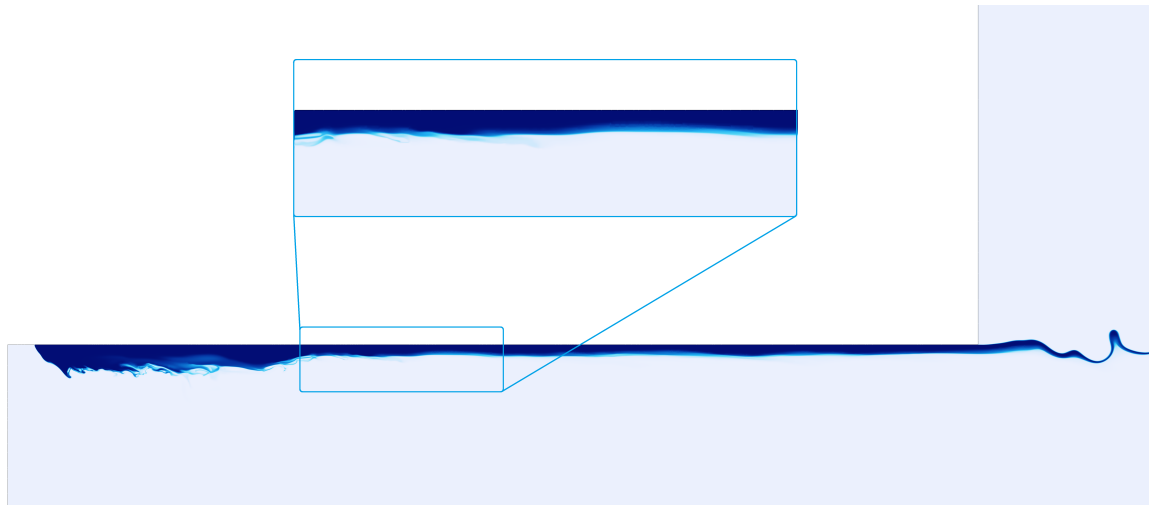
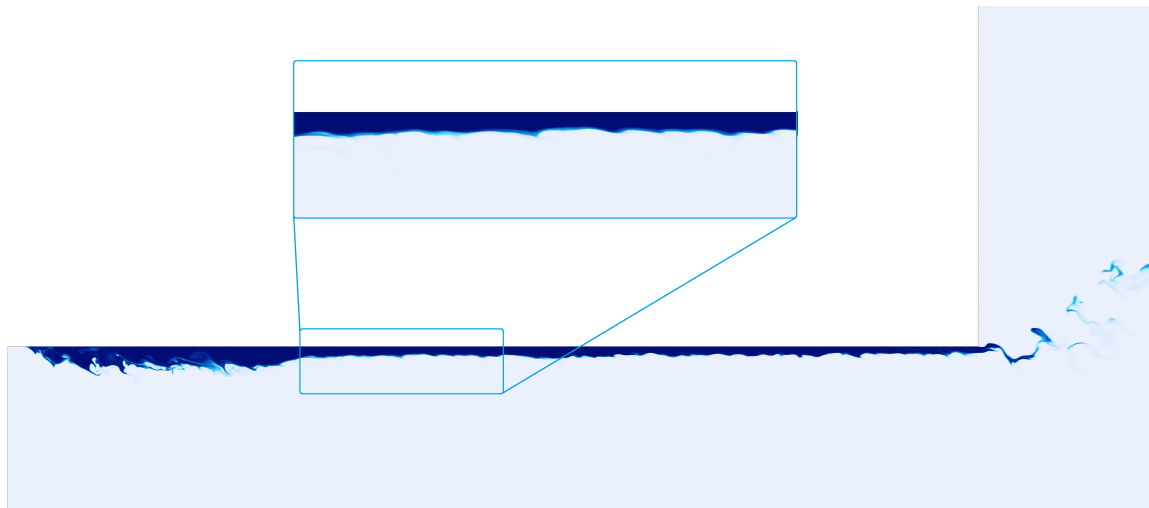


Figure 4.10: Instantaneous volume fraction snapshots with coarse mesh.



(a) RSM



(b)  $k - \omega$  SST

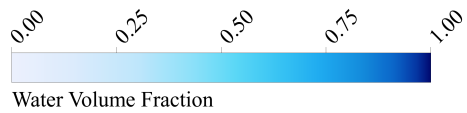


Figure 4.11: Instantaneous volume fraction snapshots with medium (a) and fine (b) mesh.

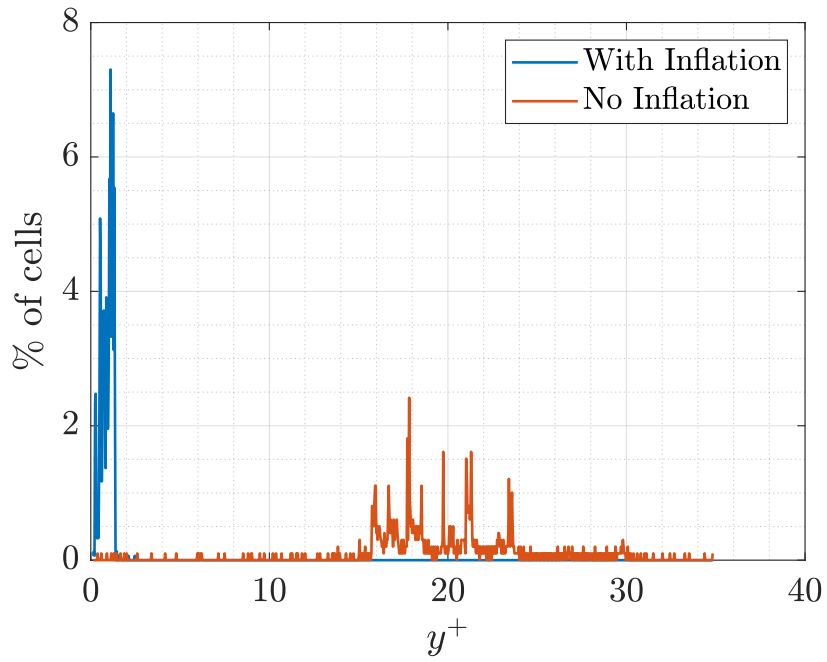


Figure 4.12: Cell distribution of  $y^+$ .

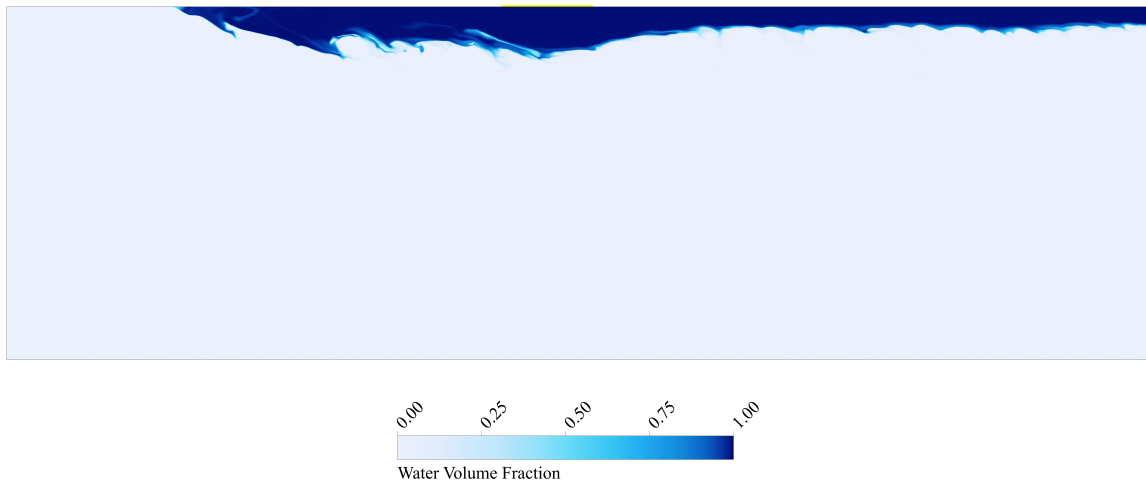


Figure 4.13: Instantaneous volume fraction snapshot –  $k - \omega$  SST with fine mesh and  $W_g = 150$  m/s.

The contour plots of the vorticity magnitude and pressure are illustrated in Figure 4.14. The formation of vortices from the interaction between gas and liquid phase is clearly

visible. The vortices are a combination of axial and swirl velocities, and rotational velocity around their core. The high vorticity zones match the low pressure zones.

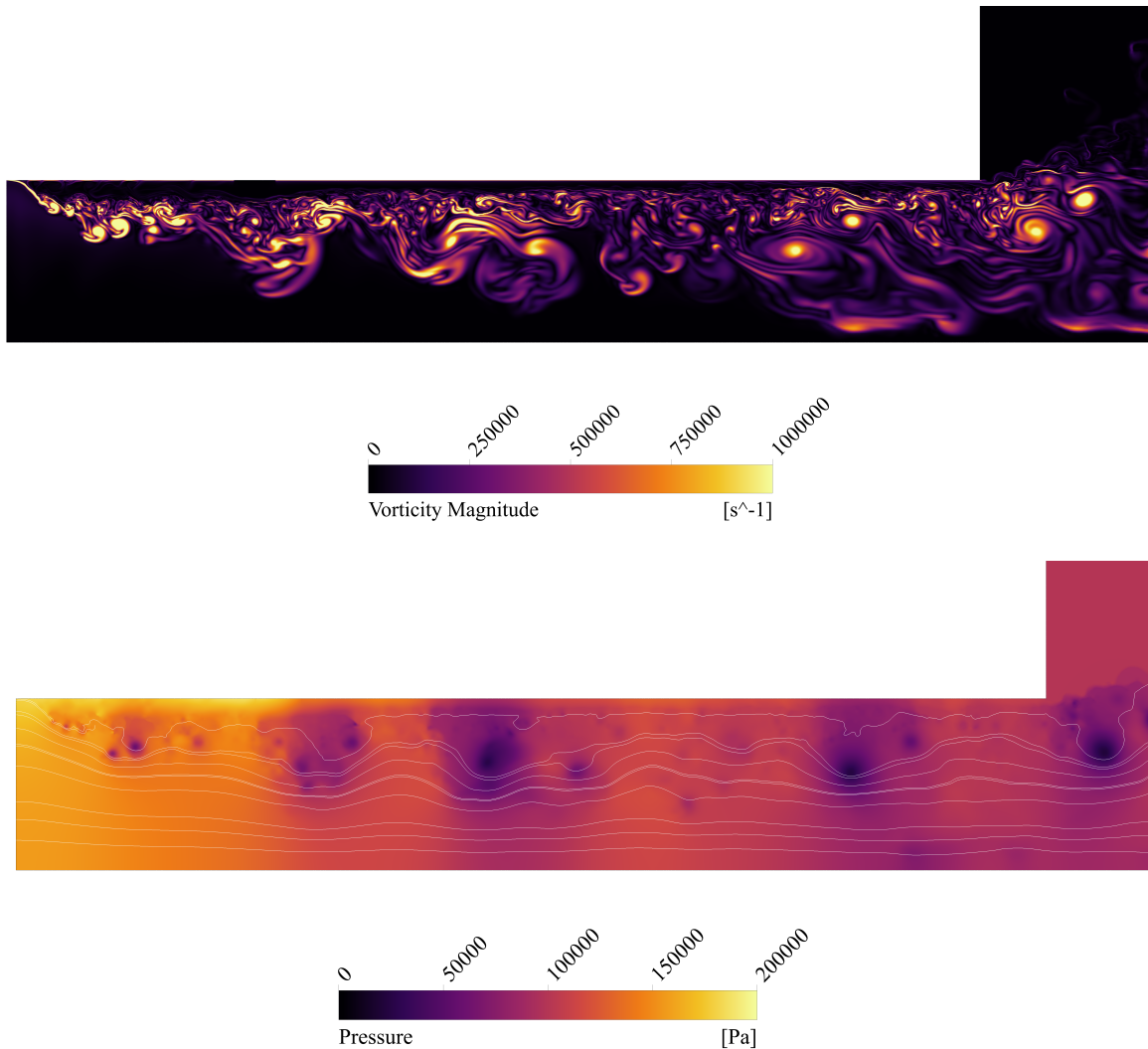


Figure 4.14: Instantaneous vorticity magnitude and pressure –  $k - \omega$  SST with fine mesh and  $W_g = 100$  m/s.

Interesting information can be derived from the time-averaged flow field. The streamlines representing the mean velocity of the liquid phase in the region between the air and water inlet are shown in Figure 4.16. Clearly, the swirling velocity is predominant in the thick liquid region where the axial velocity is slightly negative or zero. This confirms that the steady-state approach used in the theoretical derivation of the extended theory is coher-

ent. The time-averaged liquid-gas interface position for all the models used in this study is illustrated in Figure 4.15. The latter also depicts the liquid surface for the inviscid case in the CHOE configuration, which overlaps to the other curves confirming the analogous behavior within the injector.

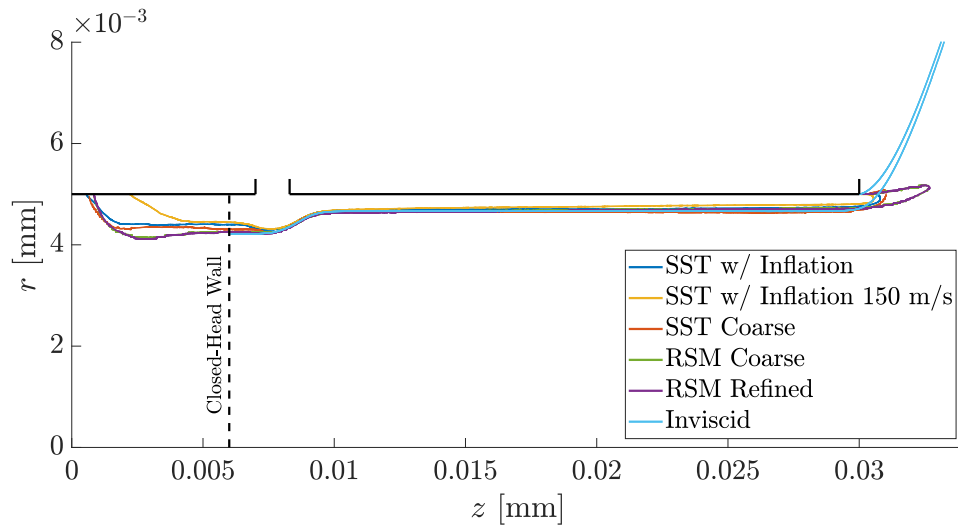
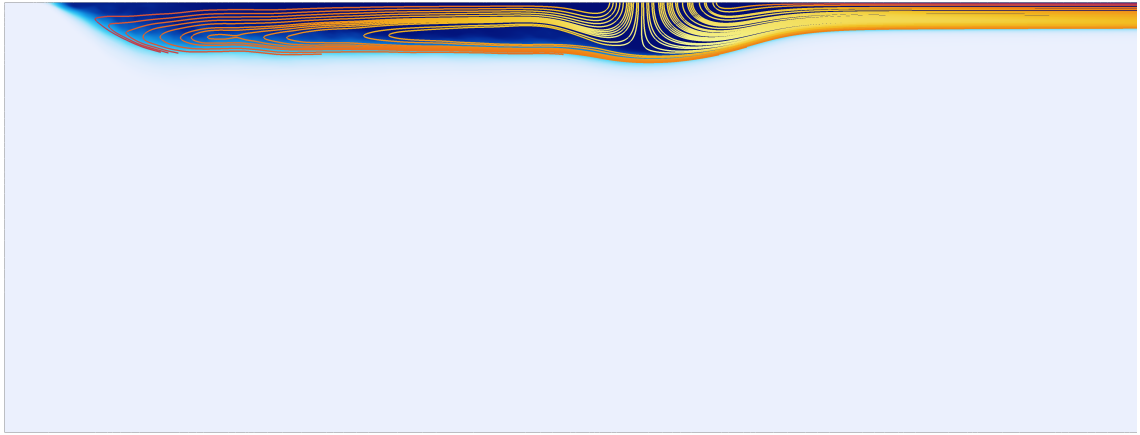
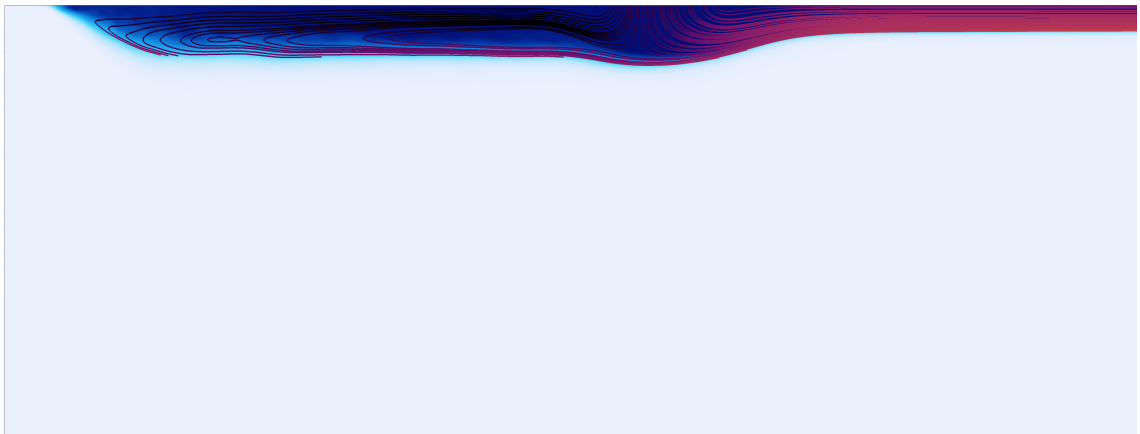


Figure 4.15: Time-averaged liquid surface for different turbulence models and grids. The dashed line coincides with the head-end wall of the CHOE injector in the inviscid case.



(a) Streamlines colored by mean swirl velocity.



(b) Streamlines colored by mean axial velocity.

Figure 4.16: Water time-averaged streamlines –  $k - \omega$  SST with fine mesh and  $W_g = 100$  m/s.

## CHAPTER 5

### RESULTS AND CONCLUSIONS

A new class of coaxial swirl injectors featured by an open-head open-end configuration was studied from a theoretical and numerical standpoint. This work provides a review and extension of the classical theory of injector dynamics aiming to obtain a model suitable for OHOE swirl injectors. The examination of the previous steady-state and dynamic theory reveals the existence of inconsistencies and typographical errors, which were addressed. Specifically, the classical model for CHOE injectors computes the oscillation amplitude of the liquid surface by taking into account the disturbance speed on a stationary liquid. In contrast, the phase shift and damping effect affecting the waves reaching the injector exit correctly consider the mean axial velocity of the liquid. On the contrary, the extended theory is consistent and incorporates the liquid axial velocity in the derivation of the wave amplitude. Furthermore, the classical theory includes a damping effect in the vorticity waves transfer function, which is not significant due to the thinner nature of the liquid film in open-end injectors. The elimination of the damping term results in a maximum discrepancy of approximately 0.3% in the transfer function amplitude and phase, confirming the negligible impact of this term.

The extension of the classical theory to OHOE injectors necessitates the inclusion of additional physical phenomena in the theoretical derivation. The effect of shear stress at the liquid-wall and gas-liquid interface is introduced in the governing equations. Previous theories rely on an artificial viscosity factor empirically derived for closed-head injectors. Furthermore, these models lack any term to address gas-liquid shear stress, given the stationary gas core. In contrast, the extended theory provides an analytical treatment of shear stress effects, resulting in a modified wave equation. The solution involves the derivation of a complex wave number that is a function of the forcing term. Consequently, this leads

to an analytical damping factor and a wave amplitude dependent on the disturbance frequency. As a result, the terms in the injector transfer function associated with the swirling chamber and the propagation of waves to the injector exit undergo modification.

The classical theory is recovered when setting the friction coefficients to zero, but the resolution of the inconsistencies in the classical model generates some discrepancies as discussed in Section 3.3. Emulating the classical theory through the extended theory, under the condition of zero gas velocity, maintains a similar trend for the transfer function compared to the earlier approach. Nevertheless, an unusual overshoot at extremely low frequencies is observed in the response function amplitude. Initially, an asymptotic approach improves this behaviour but the method is deemed inaccurate and conceptually flawed. Consequently, modified friction coefficients are introduced to appropriately correct the extended theory. The incorporation of a linear frequency dependence in the liquid-wall friction coefficient ensures consistent results with the classical model. These results are obtained through the calibration of two parameters, utilizing the classical theory as a reference. A parametric study on geometric and flow variables for frequencies below 2000 Hz reveals certain properties of the tuning coefficients. Specifically, the injector length does not influence these coefficients. Conversely, the geometric characteristic parameter  $A$  and injector pressure drop affect the tuning coefficients. The modification of  $A$  and  $\Delta p_{inj}$  leads to variations of the injector radius and flow velocities, respectively. Since these quantities contribute to the friction coefficient as part of the Reynolds number, the variability of the tuning coefficients underscores an inaccurate dependency of  $C_f$  on Reynolds. A gas velocity between 50 and 200 m/s produces a remarkably small increase of the response function amplitude. This can be attributed to the significant axial momentum flux ratio in favor of the liquid phase.

A numerical investigation was conducted through CFD simulations to provide a qualitative description of the flow physics in OHOE coaxial swirl injectors. A fraction of the tangentially injected liquid moves axially towards the injector exit, while another fraction moves upstream, opposite to the gas flow. This is caused by the higher momentum carried

by the liquid compared to the gas momentum. Consequently, a thick liquid region forms in the space between the inlets of the two fluids. In this region, the liquid exhibits a predominant swirl velocity component, as indicated by the time-averaged solutions. Overlapping the mean position of the gas-liquid interface in the OHOE injector to the inviscid solution for CHOE injectors reveals analogous behavior of the liquid film within the injector. On the contrary, the liquid spray in the OHOE configuration markedly differs from that of a closed-head injector, as evidenced by instantaneous snapshots of the volume fraction, which depict an oscillating and unstable spray. The snapshots reveal the formation of surface oscillations, accentuated by the remarkably small thickness of the liquid film in the investigated injector configuration. Furthermore, gas-liquid interaction produces intense vortices and pressure oscillations in the gas, contributing to surface oscillations. In conclusion, a higher gas velocity leads to a shorter liquid region between the two inlets and a thinner liquid film.

## 5.1 Future Work

The results of this study show that modifying the friction coefficients by introducing a frequency dependency and suitable tuning coefficients can effectively influence the transfer function amplitude and phase. Future research focusing on CFD simulations for OHOE injectors could yield valuable insights into the liquid-wall and gas-liquid friction coefficients. The numerical study may involve introducing mass flow rate oscillations at the liquid inlet to induce surface waves. By computing the injector response function, gas-liquid interaction could be analyzed across various frequencies and oscillation amplitudes. Consequently, tuning the friction coefficients to replicate the numerical results could lead to the derivation of accurate expressions for these coefficients. A study of this kind could confirm the minimal impact of the gas flow on the injector response for the velocity range studied or facilitate the modification of  $C_{f,lg}$  to counteract the damping effect of the wall. In addition, future CFD studies could examine the effects of compressibility of the gas phase on the

flow field. Regarding the theoretical approach, incorporating gas pressure oscillations in the governing equations is a prospect. Specifically, a dynamic pressure term proportional to the gas velocity and local slope of the oscillating liquid surface could potentially promote the growth of surface waves.

## REFERENCES

- [1] G. N. Abrarnovich. *Applied Gas Dynamics*. Moscow, Russia: Nauka, 1976.
- [2] Geoffrey Taylor. “The Mechanism of Swirl Atomizers”. In: *Proceedings of 7th International Congress for Applied Mechanics*. Vol. 2. London, 1948.
- [3] Vladimir Bazarov, Vigor Yang, and Puneesh Puri. “Design and Dynamics of Jet and Swirl Injectors”. In: *Liquid Rocket Thrust Chambers*. Chap. 2, pp. 19–103. eprint: <https://arc.aiaa.org/doi/pdf/10.2514/5.9781600866760.0019.0103>.
- [4] Vladimir G. Bazarov and Vigor Yang. “Liquid-Propellant Rocket Engine Injector Dynamics”. In: *Journal of Propulsion and Power* 14.5 (1998), pp. 797–806.
- [5] V. Bazarov. *Dynamics of Liquid Injectors*. Moscow: Mashinostroenie, 1979.
- [6] Yun-Jae Chung et al. “Experimental Study on Simplex Swirl Injector Dynamics with Varying Geometry”. In: *International Journal of Aeronautical and Space Sciences* 12 (Mar. 2011).
- [7] Taeock Khil et al. “Dynamic Characteristics of Simplex Swirl Injector in Low Frequency Range”. In: *Journal of Propulsion and Power* 28.2 (2012), pp. 323–333. eprint: <https://doi.org/10.2514/1.B34169>.
- [8] Taeock Khil et al. “Quantification of the transient mass flow rate in a simplex swirl injector”. In: *Measurement Science and Technology* 20.7 (June 2009), p. 075405.
- [9] Yunjae Chung et al. “Dynamic Characteristics of Open-Type Swirl Injector with Varying Geometry”. In: *Journal of Propulsion and Power* 32.3 (2016), pp. 583–591. eprint: <https://doi.org/10.2514/1.B35729>.
- [10] Seokgyu Jeong et al. “Effect of self-excited instability on single liquid swirl injector flow characteristics”. In: *Acta Astronautica* 178 (2021), pp. 452–462.
- [11] Ji-Hyuk Im et al. “Self-Pulsation Characteristics of a Swirl Coaxial Injector with Various Injection and Geometric Conditions”. In: *41st AIAA/ASME/SAE/ASEE Joint Propulsion Conference & Exhibit*. eprint: <https://arc.aiaa.org/doi/pdf/10.2514/6.2005-3749>.
- [12] Seokgyu Jeong et al. “Self-Excited Instability of Closed-Type Swirl Injector with Varying Conditions”. In: *Journal of Propulsion and Power* 36.2 (2020), pp. 285–293. eprint: <https://doi.org/10.2514/1.B37618>.

- [13] Seokgyu Jeong and Youngbin Yoon. “Sheet-breakup characteristics of a closed-type swirl injector considering internal flow instability”. In: *Acta Astronautica* 186 (2021), pp. 363–371.
- [14] Poong-Gyoo Han et al. “The Spray Characteristics of Swirl Coaxial Injectors”. In: *41st Aerospace Sciences Meeting and Exhibit*. eprint: <https://arc.aiaa.org/doi/pdf/10.2514/6.2003-490>.
- [15] Dongjun Kim et al. “Effect of Ambient Gas Density on Spray Characteristics of Swirling Liquid Sheets”. In: *Journal of Propulsion and Power* 23.3 (2007), pp. 603–611. eprint: <https://doi.org/10.2514/1.20161>.
- [16] Ji-Hyuk Im et al. “Comparative Study of Spray Characteristics of Gas-Centered and Liquid-Centered Swirl Coaxial Injectors”. In: *Journal of Propulsion and Power* 26.6 (2010), pp. 1196–1204. eprint: <https://doi.org/10.2514/1.48436>.
- [17] Yoonwan Moon, Dongjun Kim, and Youngbin Yoon. “Improved Spray Model for Viscous Annular Sheets in a Swirl Injector”. In: *Journal of Propulsion and Power* 26.2 (2010), pp. 267–279. eprint: <https://doi.org/10.2514/1.45010>.
- [18] Hongbok Park and Stephen D. Heister. “Nonlinear simulation of free surfaces and atomization in pressure swirl atomizers”. In: *Physics of Fluids* 18.5 (May 2006), p. 052103. eprint: [https://pubs.aip.org/aip/pof/article-pdf/doi/10.1063/1.2197876/15757590/052103\\\_1\\\_online.pdf](https://pubs.aip.org/aip/pof/article-pdf/doi/10.1063/1.2197876/15757590/052103\_1\_online.pdf).
- [19] M. Ismailov and S. Heister. “Dynamic Response of Rocket Swirl Injectors, Part I: Wave Reflection and Resonance”. In: *Journal of Propulsion and Power* 27.2 (2011), pp. 402–411.
- [20] M. Ismailov and S. Heister. “Dynamic Response of Rocket Swirl Injectors, Part II: Nonlinear Dynamic Response”. In: *Journal of Propulsion and Power* 27.2 (2011), pp. 412–421.
- [21] M. Ismailov. “Modeling of Classical Swirl Injector Dynamics”. PhD thesis. West Lafayette, Indiana: Purdue University, 2010.
- [22] R. Richardson. “Linear and Nonlinear Dynamics of Swirl Injectors”. PhD thesis. West Lafayette, IN: Purdue University, 2007.
- [23] Qing-fei Fu, Li-jun Yang, and Xiang-dong Wang. “Theoretical and Experimental Study of the Dynamics of a Liquid Swirl Injector”. In: *Journal of Propulsion and Power* 26.1 (2010), pp. 94–101. eprint: <https://doi.org/10.2514/1.44271>.

- [24] Qing-fei Fu, Li-jun Yang, and Yuan-yuan Qu. “Measurement of annular liquid film thickness in an open-end swirl injector”. In: *Aerospace Science and Technology* 15.2 (2011), pp. 117–124.
- [25] Qing-Fei Fu et al. “Geometrical Effects on the Fluid Dynamics of an Open-End Swirl Injector”. In: *Journal of Propulsion and Power* 27.5 (2011), pp. 929–936. eprint: <https://doi.org/10.2514/1.B34078>.
- [26] L. Yang and Q. Fu. “Theoretical Study of Dynamic Characteristic of Open-End Liquid Swirl Injector”. In: *International Astronautical Federation Paper*. IAC-06-C4.P.3.09. 2006.
- [27] Sergey Zakharov, Renith Richardson, and Stephen Heister. “Hydrodynamic Modeling of Swirl Injectors with Multiple Rows of Tangential Channels”. In: *42nd AIAA/ASME/SAE/ASEE Joint Propulsion Conference & Exhibit*. eprint: <https://arc.aiaa.org/doi/pdf/10.2514/6.2006-5202>.
- [28] Li-Jun Yang and Qing-Fei Fu. “Theoretical Investigation on the Dynamics of a Gas-Liquid Coaxial Swirl Injector”. In: *Journal of Propulsion and Power* 27.1 (2011), pp. 144–150. eprint: <https://doi.org/10.2514/1.B34004>.
- [29] Gujeong Park et al. “Characteristics of Gas-Centered Swirl-Coaxial Injector with Liquid Flow Excitation”. In: *Journal of Propulsion and Power* 35.3 (2019), pp. 624–631. eprint: <https://doi.org/10.2514/1.B36647>.
- [30] Gujeong Park et al. “Characteristics of Gas-Centered Swirl Coaxial Injector with Acoustic Excitation of Gas Flow”. In: *AIAA Journal* 55.3 (2017), pp. 894–901. eprint: <https://doi.org/10.2514/1.J055126>.
- [31] Yuchao Gao et al. “Three-dimensional simulation of a gas-centered swirl coaxial injector spray under pulsation conditions”. In: *AIP Advances* 13.5 (May 2023), p. 055302. eprint: [https://pubs.aip.org/aip/adv/article-pdf/doi/10.1063/5.0149575/17252780/055302\\_1\\_5.0149575.pdf](https://pubs.aip.org/aip/adv/article-pdf/doi/10.1063/5.0149575/17252780/055302_1_5.0149575.pdf).
- [32] Chen Chen et al. “Experimental study on the flow field distribution characteristics of a gas–liquid swirl coaxial injector under ambient pressure”. In: *Aerospace Science and Technology* 114 (2021), p. 106757.
- [33] L. Opfer, Ilia Roisman, and Cameron Tropea. “Primary Atomization in an Airblast Gas Turbine Atomizer”. In: Jan. 2013, pp. 3–27. ISBN: 978-94-007-5319-8.
- [34] Julien Carmona et al. “Lagrangian Simulation Methodology for Large-Eddy Simulations of Prefilming Air-Blast Injectors”. In: *Journal of Propulsion and Power* 39.6 (2023), pp. 856–874. eprint: <https://doi.org/10.2514/1.B39057>.

- [35] *Injector Geometry Effect on Plain Jet Airblast Atomisation*. Vol. 3: Coal, Biomass and Alternative Fuels; Combustion and Fuels; Oil and Gas Applications; Cycle Innovations. Turbo Expo: Power for Land, Sea, and Air. June 1998, V003T06A041. eprint: <https://asmedigitalcollection.asme.org/GT/proceedings-pdf/GT1998/78644/V003T06A041/2411225/v003t06a041-98-gt-445.pdf>.
- [36] Peter Stephan et al. “Experimental and Numerical Investigation of Shear-Driven Film Flow and Film Evaporation”. In: Jan. 2013, pp. 29–54. ISBN: 978-94-007-5320-4.
- [37] Umesh Bhayaraju and Christoph Hassa. “Planar liquid sheet breakup of prefilming and nonprefilming atomizers at elevated pressure”. In: *Atomization And Sprays* 19 (Dec. 2009), pp. 1147–1169.
- [38] Sebastian Gepperth et al. “Pre-filming primary atomization: Experiments and modeling”. In: Nov. 2010.
- [39] Simon Holz et al. “Close Nozzle Spray Characteristics of a Prefilming Airblast Atomizer”. In: *Energies* 12.14 (2019).
- [40] Sven Hoffmann et al. “Euler–Lagrangian simulation of the fuel spray of a planar prefilming airblast atomizer”. In: *CEAS Aeronautical Journal* 12.2 (Apr. 2021), pp. 245–259.
- [41] Abhijeet Kumar and Srikrishna Sahu. “Liquid jet breakup unsteadiness in a coaxial air-blast atomizer”. In: *International Journal of Spray and Combustion Dynamics* 10.3 (2018), pp. 211–230. eprint: <https://doi.org/10.1177/1756827718760905>.
- [42] Chuanyu Fang et al. “Aerodynamic effect on atomization characteristics in a swirl cup airblast fuel injector”. In: *Physics of Fluids* 35.10 (Oct. 2023), p. 103319. eprint: <https://pubs.aip.org/aip/pof/article-pdf/doi/10.1063/5.0170317/18173351/103319\1\5.0170317.pdf>.
- [43] Shirin Patil and Srikrishna Sahu. “Air swirl effect on spray characteristics and droplet dispersion in a twin-jet crossflow airblast injector”. In: *Physics of Fluids* 33.7 (July 2021), p. 073314. eprint: <https://pubs.aip.org/aip/pof/article-pdf/doi/10.1063/5.0054430/13830422/073314\1\online.pdf>.
- [44] Y. Ditiakin et al. *Atomization of Liquids*. 3rd. Moscow, Russia: Mashinostroenie Publication, Inc., 1987.
- [45] N. Ye. Kochin, Kibel’ I. A., and Roze N. V. *Teoreticheskaya gidromekhanika (Theoretical hydromechanics)*. T. T. M., Ogiz, 1948.

- [46] Shirin Patil and Srikrishna Sahu. “Spray characterization in a multi-jet airblast injector with swirling air crossflow”. In: *Aerospace Science and Technology* 132 (2023), p. 108085.
- [47] Takao Inamura and Nobuki Nagai. “Spray Characteristics of Liquid Jet Traversing Subsonic Airstreams”. In: *Journal of Propulsion and Power* 13.2 (1997), pp. 250–256. eprint: <https://doi.org/10.2514/2.5156>.
- [48] Kamel Sidi-Ali and Renée Gagnol. “Interfacial friction factor determination using CFD simulations in a horizontal stratified two-phase flow”. In: *Chemical Engineering Science* 65.18 (2010), pp. 5160–5169.
- [49] Xiaodong Chen and Vigor Yang. “Effect of ambient pressure on liquid swirl injector flow dynamics”. In: *Physics of Fluids* 26.10 (Oct. 2014), p. 102104. eprint: [https://pubs.aip.org/aip/pof/article-pdf/doi/10.1063/1.4899261/13798305/102104\\\_1\\\_online.pdf](https://pubs.aip.org/aip/pof/article-pdf/doi/10.1063/1.4899261/13798305/102104\_1\_online.pdf).